Characterization of Errors in Satellite-based $HCHO/NO_2$ Tropospheric Column Ratios with Respect to Chemistry, Column to PBL Translation, Spatial Representation, and Retrieval Uncertainties

Amir H. Souri[1*], Matthew S. Johnson[2], Glenn M. Wolfe[3], James H. Crawford[4], Alan Fried[5], Armin Wisthaler[6,7], William H. Brune[8], Donald R. Blake[9], Andrew J. Weinheimer[10], Tijl Verhoelst[11], Steven Compernolle[11], Gaia Pinardi[11], Corinne Vigouroux[11], Bavo Langerock[11], Sungyeon Choi[3,12], Lok Lamsal[3,13], Lei Zhu[14,15], Shuai Sun[14,15], Ronald C. Cohen[16,17], Kyung-Eun Min[18], Changmin Cho[18], Sajeev Philip[19], Xiong Liu[1], and Kelly Chance[1]

[1]Atomic and Molecular Physics (AMP) Division, Center for Astrophysics | Harvard & Smithsonian, Cambridge, MA, USA
[2]Earth Science Division, NASA Ames Research Center, Moffett Field, CA, USA
[3]NASA Goddard Space Flight Center, Greenbelt, MD, USA
[4]NASA Langley Research Center, Hampton, VA, USA
[5]Institute of Arctic & Alpine Research, University of Colorado, Boulder, CO, USA
[6]Institute for Ion Physics and Applied Physics, University of Innsbruck, Technikerstrasse 25, 6020 Innsbruck, Austria
[7]Department of Chemistry, University of Oslo, P.O. box 1033, Blindern, 0315 Oslo, Norway
[8]Department of Meteorology and Atmospheric Science, Pennsylvania State University, University Park, PA, USA
[9]Department of Chemistry, University of California, Irvine, CA, USA
[10]National Center for Atmospheric Research, Boulder, CO, USA
[11]Royal Belgian Institute for Space Aeronomy (BIRA-IASB), Ringlaan 3, 1180 Uccle, Belgium
[12]Science Systems and Applications, Inc., Lanham, MD 20706, USA
[13]Universities Space Research Association, Columbia, MD 21046, USA
[14]School of Environmental Science and Engineering, Southern University of Science and Technology, Shenzhen, Guangdong, China
[15]Guangdong Provincial Observation and Research Station for Coastal Atmosphere and Climate of the Greater Bay Area, Shenzhen, Guangdong, China
[16]Department of Earth and Planetary Science, University of California Berkeley, Berkeley, CA 94720, USA
[17]Department of Chemistry, University of California Berkeley, Berkeley, CA 94720, USA
[18]School of Earth Sciences and Environmental Engineering, Gwangju Institute of Science and Technology, Gwangju, South Korea
[19]Centre for Atmospheric Sciences, Indian Institute of Technology Delhi, New Delhi, India

* Corresponding Author: ahsouri@cfa.harvard.edu

Abstract.

The availability of formaldehyde (HCHO) (a proxy for volatile organic compound reactivity) and nitrogen dioxide (NO_2) (a proxy for nitrogen oxides) tropospheric columns from Ultraviolet-Visible (UV-Vis) satellites has motivated many to use their ratios to gain some insights into the near-surface ozone sensitivity. Strong emphasis has been placed on the challenges that come with transforming what is being observed in the tropospheric column to what is actually in the planetary boundary layer (PBL) and near to the surface; however, little attention has been paid

to other sources of error such as chemistry, spatial representation, and retrieval uncertainties. Here we leverage a wide spectrum of tools and data to carefully quantify those errors.

Concerning the chemistry error, a well-characterized box model constrained by more than 500 hours of aircraft data from NASA's air quality campaigns is used to simulate the ratio of the chemical loss of HO_2+RO_2 (LROx) to the chemical loss of NO_x (LNOx). Subsequently, we challenge the predictive power of HCHO/NO_2 ratios (FNRs), which are commonly applied in current research, at detecting the underlying ozone regimes by comparing them to LROx/LNOx. FNRs show a strongly linear (R^2=0.94) relationship to LROx/LNOx in the log-log scale. Following the baseline (i.e., ln(LROx/LNOx) = -1.0±0.2) with the model and mechanism (CB06, r2) used for segregating NOx-sensitive from VOC-sensitive regimes, we observe a broad range of FNR thresholds ranging from 1 to 4. The transitioning ratios strictly follow a Gaussian distribution with a mean and standard deviation of 1.8 and 0.4, respectively. This implies that FNR has an inherent 20% standard error (1-sigma) resulting from not being able to fully describe the ROx-HOx cycle. We calculate high ozone production rates (PO_3) dominated by large HCHO×NO_2 concentration levels, a new proxy for the abundance of ozone precursors. The relationship between PO_3 and HCHO×NO_2 becomes more pronounced when moving towards NOx-sensitive regions due to non-linear chemistry; our results indicate that there is fruitful information in the HCHO×NO_2 metric that has not been utilized in ozone studies. The vast amount of vertical information on HCHO and NO_2 concentration from the air quality campaigns enables us to parameterize the vertical shapes of FNRs using a second-order rational function permitting an analytical solution for an altitude adjustment factor to partition the tropospheric columns to the PBL region. We propose a mathematical solution to the spatial representation error based on modeling isotropic semivariograms. With respect to a high-resolution sensor like TROPOspheric Monitoring Instrument (TROPOMI) (>5.5×3.5 km^2), Ozone Monitoring Instrument (OMI) loses 12% of spatial information at its native resolution. A pixel with a grid size of 216 km^2 fails at capturing ~65% of the spatial information in FNRs at a 50 km length scale comparable to the size of a large urban center (e.g., Los Angeles). We ultimately leverage a large suite of in-situ and ground-based remote sensing measurements to draw the error distributions of daily TROPOMI and OMI tropospheric NO_2 and HCHO columns. At 68% confidence interval (1 sigma) errors pertaining to daily TROPOMI observations, either HCHO or tropospheric NO_2 columns should be above 1.2-1.5×10^{16} molec.cm^{-2} to attain 20-30% standard error in the ratio. This level of error is almost non-achievable with OMI given its large error in HCHO.

The satellite column retrieval error is the largest contributor to the total error (40-90%) in the FNRs. Due to a stronger signal in cities, the total relative error (<50%) tends to be mild, whereas areas with low vegetation and anthropogenic sources (e.g., Rocky Mountains) are markedly uncertain (>100%). Our study suggests that continuing development in the retrieval algorithm and sensor design and calibration is essential to be able to advance the application of FNRs beyond a qualitative metric.

1. Introduction

Accurately representing the near-surface ozone (O_3) sensitivity to its two major precursors, nitrogen oxides (NOx) and volatile organic compounds (VOCs), is an imperative step in understanding non-linear chemistry associated with ozone production rates in the atmosphere. While it is often tempting to characterize an airshed as NOx or VOC-sensitive, both conditions are expected as VOC-sensitive (ozone production rates sensitive to VOC) conditions near NOx sources transition to NOx-sensitive (ozone production rates sensitive to NOx) conditions downwind as NOx dilutes. Thus, reducing the footprint of ozone production can mostly be

achieved through NOx reductions. VOCs are key to determining both the location and peak in ozone production which varies nonlinearly to the NOx abundance. Thus, knowledge of the relative levels of NOx and VOCs informs the trajectory of ozone production and expectations of where peak ozone will occur as emissions change. While the near-surface ambient nitrogen dioxide (NO_2) concentrations are regularly monitored by a large number of surface stations, the measurements of several VOCs with different reactivity rates with respect to hydroxyl (OH), are not routinely available. As such, our knowledge on where and when ozone production rates are elevated, and their quantitative dependence on a long list of ozone precursors, is fairly limited, except for observationally-rich air quality campaigns. This limitation has prompted several studies such as Sillman et al. (1990), Tonnesen and Dennis (2000a,b), and Sillman and He (2002) to investigate if the ratio of certain measurable compounds can diagnose ozone regimes meaning if the ozone production rate is sensitive to NOx (i.e., NOx-sensitive) or VOC (i.e., VOC-sensitive). Sillman and He (2002) suggested that H_2O_2/HNO_3 was a robust measurable ozone indicator as this ratio could well describe the chemical loss of HO_2+RO_2 (LROx) to the chemical loss of NOx (LNOx) controlling the O_3-NOx-VOC chemistry (Kleinman et al., 2001). Nonetheless, both H_2O_2 and HNO_3 measurements are limited to few spatially-sparse air quality campaigns.

Formaldehyde (HCHO) is an oxidation product of VOCs and its relatively short lifetime (~1-9 hr) makes the location of its primary and secondary sources rather identifiable (Seinfield and Pandis, 2006; Fried et al., 2020). Fortunately, monitoring HCHO abundance in the atmosphere has been a key goal of many Ultraviolet-Visible (UV-Vis) viewing satellites for decades (Chance et al., 1991; Chance et al., 1997; Chance et al., 2000; González Abad et al., 2015; De Smedt et al., 2008, 2012, 2015, 2018, 2021) with reasonable spatial coverage. Additionally, the strong absorption of NO_2 in the UV-Vis range has permitted measurements of NO_2 columns from space (Martin et al., 2002; Boersma et al., 2004, 2007, 2018).

Advancements in satellite remote-sensing of these two key compounds have encouraged many studies to elucidate if the ratio of $HCHO/NO_2$ (hereafter FNR) could be a robust ozone indicator (Tonnensen and Dennis, 2000b; Martin et al. 2004, Duncan et al., 2010). Most studies using the satellite-based FNR columns attempted to provide a qualitative view of the underlying chemical regimes (e.g., Choi et al., 2012; Choi and Souri, 2015a,b; Jin and Holloway, 2015; Souri et al., 2017; Jeon et al., 2018; Lee et al., 2021). Relatively few studies (Duncan et al., 2010; Jin et al., 2017; Schroeder et al., 2017; Souri et al., 2020) have carefully tried to provide a quantitative view of the usefulness of the ratio. For the most part, the inhomogeneous vertical distribution of FNR in columns has been emphasized. Jin et al. (2017) and Schroeder et al. (2017) showed that differing vertical shapes of HCHO and NO_2 can cause the vertical shape of FNR not to be consistent throughout the troposphere leading to a variable relationship between what is being observed from the satellite and what is actually occurring in the lower atmosphere. Jin et al. (2017) calculated an adjustment factor to translate the column to the surface using a relatively coarse global chemical transport model. The adjustment factor showed a clear seasonal cycle stemming from spatial and temporal variability associated with the vertical sources and sinks of HCHO and NO_2, in addition to the atmospheric dynamics. In a more data driven approach, Schroeder et al. (2017) found that the detailed differences in the boundary layer vertical distributions of HCHO and NO_2 lead to a wide range of ambiguous ratios. Additionally, ratios were shown to shift on high ozone days, raising questions regarding the value of satellite averages over longer timescales. A goal for our research is to put together an integrated and data-driven mathematical formula to translate the tropospheric column to the planetary boundary layer (PBL), exploiting the abundant aircraft measurements available during ozone seasons.

Using observationally-constrained box models, Souri et al. (2020) demonstrated that there was a fundamentally inherent uncertainty related to the ratio originating from the chemical dependency of HCHO on NO_x (Wolfe et al., 2016). In VOC-rich (poor) environments, the transitioning ratios from NOx-sensitive to VOC-sensitive occurred in larger (smaller) values than the conventional thresholds defined in Duncan et al. (2010) due to an increased (dampened) HCHO production induced by NOx. To account for the chemical feedback and to prevent a wide range of thresholds on segregating NOx-sensitive from VOC-sensitive regions, Souri et al. (2020) suggested using a first-order polynomial matched to the ridgeline in $P(O_3)$ isopleths. Their study illuminated the fact that the ratio suffers from an inherit chemical complication. However, Souri et al. (2020) did not quantify the error and their work was limited to a subset of atmospheric condition. To challenge the predictive power of FNR from chemistry perspective, we will take advantage of a large suite of datasets to make maximum use of varying meteorological and chemical conditions.

Not only are satellite-based column measurements unable to resolve the vertical information of chemical species in the tropospheric column, but they are also unable to resolve the horizontal spatial variability due to their spatial footprint. The larger the footprint is, the more horizontal information is blurred out. For instance, Souri et al. (2020) observed a substantial spatial variance (information) in FNR columns at the spatial resolution of 250×250 m^2 observed by an airborne sensor over Seoul, South Korea. It is intuitively clear that a coarse resolution sensor would lose a large degree of spatial variance (information). This error, known as the spatial representation error, has not been studied with respect to FNR. We will leverage what we have learned from Souri et al. (2022), which modeled the spatial heterogeneity in discrete data using geostatistics, to quantify the spatial representation error in the ratio over an urban environment.

A longstanding challenge is to have a reliable estimate on the satellite retrieval errors of tropospheric column NO_2 and HCHO. Significant efforts have been made recently to assemble, analyze, and estimate the retrieval errors for two key satellite sensors, TROPOspheric Monitoring Instrument (TROPOMI) and Ozone Monitoring Instrument (OMI), using various in-situ measurements (Verhoelst et al., 2021; Vigouroux et al., 2020, Choi et al., 2020; Laughner et al., 2019; Zhu et al., 2020). In this study, we will exploit paired comparisons from some of these new studies to propagate individual uncertainties in HCHO and NO_2 to the FNR errors.

The overarching science goal of this study is to address the fact that the accurate diagnosis of surface O_3 photochemical regimes is impeded by numerous uncertainty components, which will be addressed in the current paper, and can be classified into four major categories: i) inherent uncertainties associated with the approach of FNRs to diagnose local O_3 production and sensitivity regimes, ii) translation of tropospheric column satellite retrievals to represent PBL- or surface-level chemistry, iii) spatial representativity of ground pixels of satellite sensors, and iv) uncertainties associated with satellite-retrieved column-integrated concentrations of HCHO and NO_2. We will address all of these sources of uncertainty using a broad spectrum of data and tools.

Our paper is organized with the following sections. Section 2 describes the chemical box model setup and data applied. Sections 3.1 to 3.4 deal with chemistry aspects of FNRs and show the results from a box model. Section 3.5 introduces a data-driven framework to transform the FNR tropospheric columns to the PBL region. Section 3.6 offers a new way to quantify the spatial representation error in satellites. Section 3.7 deals with the satellite error characterization and their impacts on the ratio. Section 3.8 summarizes the fractional contribution of each error to the combined error. Finally, Sect. 4 provides a summary and conclusions of the study.

2. Photochemical Box Modeling and Aircraft Data Used

To quantify the uncertainty of FNR from a chemistry perspective, and to obtain several imperative parameters including the calculated ozone production rates, and the loss of NO_x (LNO_x) and RO_x (LRO_x), we utilize the Framework for 0-D Atmospheric Modeling (F0AM) v4 (Wolfe et al., 2016). We adopt the Carbon Bond 6 (CB06, r2) chemical mechanism and heterogenous chemistry is not considered in our simulations. The model is initialized with the measurements of several compounds, many of which constrain the model by being held constant for each timestep (see Table 1).

Figure 1 shows the map of data points from Deriving Information on Surface Conditions from Column and Vertically Resolved Observations Relevant to Air Quality (DISCOVER-AQ) Baltimore-Washington (2011), DISCOVER-AQ Houston-Texas (2013), DISCOVER-AQ Colorado (2014), and Korea United States Air Quality Study (KORUS-AQ) (2016). Meteorological inputs come from the observed pressure, temperature, and relative humidity. The measurements of photolysis rates are not available for all photolysis reactions; therefore, our initial guess of those rates comes from a look-up-table populated by the National Center for Atmospheric Research (NCAR) Tropospheric Ultraviolet And Visible (TUV) model calculations. These values are a function of solar zenith angle, total ozone column density, surface albedo, and altitude. We set the total ozone column and the surface albedo to fixed numbers of 325 (Dobson) DU and 0.15, respectively. The initial guess is then corrected by applying the ratio of observed photolysis rates of NO_2+hv (jNO_2) and/or O_3+hv (jO^1D) to the calculated ones to all j-values (i.e., wavelength independent). If both observations of jNO_2 and jO^1D are available, the correction factor is averaged. The KORUS-AQ campaign is the only one that provides jO^1D measurements; therefore the use of the wavelength-independent correction factor based on the observed to calculated jNO_2 values for all j-values including jO^1D is a potential source of error in the model especially when aerosols are present. The model calculations are based on the observations merged to a temporal resolution varying from 10 to 15 seconds. Each calculation was run for five consecutive days with an integration time of 1 hour to approach diel steady state. We test the number of solar cycle against ten days on the KORUS-AQ setup, and observe no noticeable difference in simulated OH and HCHO (Figure S1) indicating that five solar cycles suffice. Some secondarily-formed species must be unconstrained for the purpose of model validation. Therefore, the concentrations of several secondarily-formed compounds such as HCHO and PAN are unconstrained. Nitric oxide (NO) and NO_2 are also allowed to cycle, while their sum (i.e., NOx) is constrained. Because the model does not consider various physical loss pathways including deposition and transport, which vary by time and space, we oversimplify their physical loss through a first-order dilution rate set to 1/86400-1/43200 s^{-1} (i.e., 24- or 12-hr lifetime), which in turn prevents relatively long-lived species from accumulating over time. Our decision on unconstraining HCHO, a pivotal compound impacting the simulation of HOx, may introduce some systematic biases in the simulation of radicals determining ozone chemistry (Schroeder et al., 2020). Therefore, to mitigate the potential bias in HCHO, we set the dilution factor to maintain the campaign-averaged bias in the simulated HCHO with respect to observations of less than 5%. However, it is essential to recognize that HCHO can fluctuate freely for each point measurement because the dilution constraint is set to a fixed value for an individual campaign. Each time tag is independently simulated meaning we do not initialize the next run using the simulated values from the previous one; this in turn permits parallel computation. Regarding the KORUS-AQ campaign where HOx observations were available, we only ran the model for data points with HOx measurements. Similar to Souri et al. (2020), we filled gaps in VOC observations with a bilinear interpolation method with no

extrapolation allowed. In complex polluted atmospheric conditions such as that over Seoul, South Korea, Souri et al. (2020) observed that this simplistic treatment yielded comparable results with respect to the NASA LaRC model (Schroeder et al. 2020) which incorporated a more comprehensive data harmonization. to Table 1 lists the major configuration along with the observations used for the box model.

Several parameters are calculated based on the box model outputs. LRO_x is defined through the sum of primarily radical-radical reactions:

$$LRO_x = k_{HO_2+HO_2}[HO_2]^2 + \sum k_{RO_{2i}+HO_2}[RO_{2i}][HO_2] + \sum k_{RO_{2i}+RO_{2i}}[RO_{2i}]^2 \quad (1)$$

where k is the reaction rate constant. LNO_x mainly occurs via the NO_2+OH reaction:

$$LNO_x = k_{OH+NO_2+M}[OH][NO_2][M] \quad (2)$$

where M is a third body. We calculate $P(O_3)$ by subtracting the ozone loss pathways dictated by HO_x ($HO+HO_2$), NO_2+OH, O_3 photolysis, ozonolysis, and the reaction of $O(^1D)$ with water vapor from the formation pathways through the removal of NO via HO_2 and RO_2:

$$P(O_3) = k_{HO_2+NO}[HO_2][NO] + \sum k_{RO_{2i}+NO}[RO_{2i}][NO] - k_{OH+NO_2+M}[OH][NO_2][M] - P(RONO_2) - k_{HO_2+O_3}[HO_2][O_3] - k_{OH+O_3}[OH][O_3] - k_{O(^1D)+H_2O}[O(^1D)][H_2O] - L(O_3 + alkenes) \quad (3)$$

3. Results and Discussion

3.1. Box Model Validation

There are uncertainties associated with the box model (e.g., Brune et al., 2022; Zhang et al., 2021; Lee et al., 2021) which can be attributed to: i) the lack of inclusion of physical processes such as entrainment/detrainment and diffusion, ii) discounting the heterogenous chemistry, iii) invalid assumption of the diel steady state in areas close to large emission sources or in photochemically less active environments (Thornton et al., 2002; Souri et al., 2021), iv) errors in the chemical mechanism, and v) errors in the measurements. These limitations necessitate a thorough validation of the model using unconstrained observations. While models have been known for a long time to not be 100% accurate (Box, 1976), it is important to characterize whether the model can effectively represent reality. For instance, if the simulated HCHO is poorly correlated with observations and/or displayed large magnitude biases, it will be erroneous to assume that the sources of HCHO along with relevant chemical pathways are appropriate. It is important to acknowledge that the VOC constraints for these model calculations are incomplete, especially for the DISCOVER-AQ campaigns which lacked comprehensive VOC observations. Nevertheless, we will show that the selected VOCs are sufficient to reproduce a large variance (>70%) in observed HCHO.

We diagnose the performance of the box model by comparing the simulated values of five compounds to observations: HCHO, NO, NO_2, PAN, hydroperoxyl radical (HO_2), and OH. Figure 2 depicts the scatterplot of the comparisons along with several statistics. HCHO observations are usually constrained in box models to improve the representation of HO_2 (Schroeder et al., 2017; Souri et al., 2020; Brune et al., 2022); however, this constraint may mask the realistic characterization of the chemical mechanism with respect to the treatment of VOCs. Additionally,

it is important to know if the sources of HCHO are adequate. Therefore, we detach the model from this constraint to carry out a more fair and stringent validation.

Concerning HCHO, our model does have considerable skill at reproducing the variability of observed HCHO (R^2=0.73). To evaluate if this agreement is accidentally caused by the choice of the dilution factor and to identify if our VOC treatment is inferior compared to the one adopted in the NASA LaRC (Schroeder et al., 2021), we conducted three sets of sensitivity tests for the KORUS-AQ campaign, including ones with and without considering a dilution factor and another one without HNO_3 and H_2O_2 constraints (Figure S2). When not considering a dilution factor results in no difference in the variance in HCHO captured by our model (R^2=0.81). Our model without the dilution factor is still skillful at replicating the magnitude of HCHO with less than 12% bias. It is because of this reason that the optimal dilution factor for each camping is within 12 hr to 24 hr which is not different than other box modeling studies (e.g., Brune et al., 2022; Miller and Brune, 2022). We observed no difference in the simulated HCHO when HNO_3 and H_2O_2 values were not constrained. The unconstrained NASA LaRC setup oversampled at 10-sec frequency captures 86% variance in the measurements, only slightly (6%) outperforming our result. However, the unconstrained NASA LaRC setup greatly underestimates the magnitude of HCHO compared to our model results.

The model performs well with regards to the simulation of NO (R^2=0.89) and NO_2 (R^2=0.99) in the log scale. Immediately evident is the underestimation of NO in highly polluted regions contrary to an overestimation in clean ones. This discrepancy leads to an underestimation (overestimation) of NO/NO_2 in polluted (clean) regions. The primary drivers of NO/NO_2 are jNO_2 and O_3 both of which are constrained in the model. What can essentially deviate the partitioning between NO and NO_2 from that of observations in polluted areas is the assumption of the diel steady state which is rarely strictly valid where measurements are close to large emitters. The overestimation of NO in low NO_x areas is often blamed on the lack of chemical sink pathways of NO in chemical mechanisms (e.g., Newland et al., 2021). A relatively reasonable performance of PAN (R^2=0.63) is possibly due to constraining some of the oxygenated VOCs such as acetaldehyde. Xu et al. (2021) observed a strong dependency of PAN concentrations on NO/NO_2 ratios. Smaller NO/NO_2 ratios are usually associated with larger PAN mixing ratios because NO can effectively remove peroxyacetyl radicals. We observe an overestimation of PAN (0.27 ppbv) possibly due to an underestimation of NO/NO_2. Moreover, we should not rule out the impact of the first-order dilution factor which was only empirically set in this study. For instance, if we ignore the dilution process for the KORUS-AQ campaign, the bias of the model in terms of PAN will increase by 33% resulting in a poor performance (R^2=0.40) (Figure S3). We notice that this poor performance primarily occurs for high altitude measurements where PAN is thermally stable (Figure S4); therefore, this does not impact the majority of rapid atmospheric chemistry occurring in the lower troposphere such the formation of HCHO. Schroeder et al. (2020) found that proper simulation of PAN in the polluted PBL during KORUS-AQ required a first-order loss rate based on thermal decomposition at the average PBL temperature, which was more realistic than the widely varying local PAN lifetimes associated with temperature gradients between the surface and the top of the PBL. This solution is computationally equivalent to the dilution rate used in this study.

KORUS-AQ was the only field campaign providing OH and HO_2 measurements. Concerning HO_2, former studies such as Schroeder et al. (2017), Souri et al. (2020), and Brune et al. (2022) managed to reproduce HO_2 mixing ratios with R^2 ranging from 0.6 to 0.7. The performance of our model (R^2=0.66) is similar to these past studies with near negligible biases

(<1%). One may argue that the absence of the HO_2 uptake by aerosols is contributing to some of the discrepancies we observe in the HO_2 comparison. Brune et al. (2022) provided compelling evidence showing that the consideration of the HO_2 uptake made their results significantly inconsistent with the observations suggesting that the HO_2 uptake might have been inconsequential during the campaign. Our model manages to reproduce 64% of the variance of observed OH outperforming the simulations presented in Souri et al. (2020) and Brune et al. (2022) by >10%. The slope (= 1.03) is not too far from the identity line indicating that our box model systematically overestimates OH by 0.62 10^6 cm^{-3}. This may be attributed to a missing OH sink in the mechanism or the lack of inclusion of some VOCs. A sensitivity test involving removing the first-order dilution process demonstrates that the simulation of HOx is rather insensitive to this parameter (Figure S5). This might be caused by the fact that the simulated HCHO already agrees relatively well with the observations without the dilution factor. In general, the model performance is consistent, or outperforms, results from recent box modelling studies which is an indication of it being at least roughly representative of the real-world ozone chemistry and sensitivity regimes.

3.2. Can HCHO/NO_2 ratios fully describe the HOx-ROx cycle?

Kleinman et al. (2001) demonstrated that LROx/LNOx is the most robust ozone regime indicator. Thus, the predictive power of FNR at detecting the underlying chemical conditions can be challenged by comparing FNR to LROx/LNOx. Ideally, if they show a strong degree of correspondence (i.e., R^2=1.0), we can confidently say that FNR can realistically portray the chemical regimes. Any divergence of these two quantities is indicative of inadequacy of the FNR indicator. Souri et al. (2020) observed a strong linear relationship between the logarithmic transformed FNR and those of LROx/LNOx. Our analysis in this study will be based upon the simulated values to ensure that the relationship is coherent based on a realization from the well-characterized box model. As pointed out by Schroeder et al. (2017) and Souri et al. (2020), a natural logarithm of LROx/LNOx roughly equal to -1.0 (i.e., LROx/LNOx = 0.35-0.37) perceptibly separates VOC-sensitive from NOx-sensitive regimes, which would make this threshold the baseline of our analysis.

Figure 3 demonstrates the log-log relationship of LROx/LNOx and FNR, and $P(O_3)$, from all four air quality campaigns. The log-log relationships from each individual campaign are shown in Figure S6-S9. We overlay the LROx/LNOx baseline threshold along with two commonly used thresholds for FNR suggested by Duncan et al. (2010); they defined the VOC-sensitive regimes if FNR<1 and the NO_x-sensitive ones if FNR>2. Any region undergoing a value between these thresholds is unlabeled and considered to be in a transitional regime. The size of each data point is proportional to the HCHO×NO_2 concentration magnitude. One striking finding from this plot is that there is indeed a strong linear relationship between the logarithmic-transformed LROx/LNOx and FNR (R^2=0.91). A strong linear relationship between the two quantities in the log-log scale is indicative of a power law dependence (i.e., $y=ax^b$). A strong power law dependency means that these two quantities have a poor correlation at their low and high values. This is mainly caused by the fact that HCHO does not fully describe VOC reactivity rates in rich and poor VOC environments (Souri et al., 2020). A question is what range of FNR will fall in ln(LROx/LNOx) = -1.0±0.2? Following the baseline, the transitioning ratios follow a normal distribution with a mean of 1.8, a standard deviation of 0.4, and a range from 1 to 4 (Figure S10). We define the chemical error in the application of FNR to separate the chemical regimes as the relative error standard deviation (i.e., σ/μ) of the transitioning ratios leading to ~ 20%. These numbers are based on a single model realization and can change if a different mechanism is used; nonetheless, the model has considerable skill at reproducing many different unconstrained compounds, especially OH,

suggesting that it is a rather reliable realization. The comparison of the transitioning FNRs to the NO_2 concentrations suggests no correlation (r=0.02) whereas there is a linear correlation between the transitioning ratios and the HCHO concentrations (r=0.56). This tendency reinforces the study of Souri et al. (2020) who, primarily due to the HCHO-NO_2 feedback, observed a larger FNR threshold in VOC-rich environments to be able to detect the chemical regimes.

3.3. Large PO_3 rates occur in regions with large HCHO×NO_2 concentrations when moving towards NOx-sensitive regions

A striking and perhaps intuitive tendency observed from Figure 3 is that large PO_3 rates are mostly tied to higher HCHO×NO_2. But this relationship gradually weakens as we move towards VOC-sensitive regions (smaller LROx/LNOx ratios). This is a textbook example of non-linear ozone chemistry. In VOC-sensitive areas, PO_3 can be strongly inhibited by NO_2+OH and the formation of organic nitrates despite the abundance of the precursors. In application of remote-sensing of ozone precursors, the greatest unused metric describing the mass of the ozone precursors is HCHO×NO_2. However, this metric should only be used in conjunction with FNR. To demonstrate this, based on what the baseline (LROx/LNOx) suggests against thresholds on FNRs defined by Duncan et. al. (2010), we group the data into four regions namely as NOx-sensitive – NOx-sensitive, NOx-sensitive–transitional, VOC-sensitive–transitional, and VOC-sensitive–VOC-sensitive. A different perspective into this categorization is that the transitional regimes are a weaker characterization of the main regime; for instance, NOx-sensitive–transitional regions are less NOx-sensitive than NOx-sensitive – NOx-sensitive. Subsequently, the cumulative distribution functions (CDFs) of PO_3 and HCHO×NO_2 with respect to the aforementioned groups are calculated, which is shown in Figure 4. Regarding NOx-sensitive—NOx-sensitive regions, we see the PO_3 CDF very quickly converging to the probability of 100% indicating that the distribution of PO_3 is skewed towards very low values. The median of PO_3 for this particular regime (where CDF = 50%) is only 0.25 ppbv/hr. This agrees with previous studies such as Martin et al. (2002), Choi et al. (2012), Jin et al. (2017), and Souri et al. (2017) reporting that NOx-sensitive regimes dominate in pristine areas. The PO_3 CDFs between NOx-sensitive—transitional and VOC-sensitive—VOC-sensitive are not too distinct, whereas their HCHO×NO_2 CDFs are substantially different. The non-linear ozone chemistry suppresses PO_3 in highly VOC-sensitive areas such that those values are not too different than those in mildly polluted areas (NOx-sensitive—transitional). Perhaps the most interesting conclusion from this figure is that elevated PO_3 values (median = 4.6 ppbv/hr), a factor of two larger than two previous regimes, are mostly found in VOC-sensitive—transitional. This is primary due to two causes: i) this particular regime is not strongly inhibited by the nonlinear chemistry, particularly NO_2+OH, and ii) it is associated with abundant precursors evident in the median of HCHO×NO_2 being as three times as large of those in NOx-sensitive—transitional. This tendency illustrates the notion of the non-linear chemistry and how this may affect regulations. Simply knowing where the regimes are might not suffice to pinpoint the peak of PO_3, as this analysis suggests that we need to take both FNR and HCHO×NO_2 into consideration; both metrics are readily accessible from satellite remote-sensing sensors.

3.4. Can we estimate PO_3 using the information from HCHO/NO_2 and HCHO×NO_2?

It may be advantageous to construct an empirical function fitted to these two quantities and elucidate the maximum variance (information) we can potentially gain to recreate PO_3. After several attempts, we found a bilinear function ($z=a_0+a_1x+a_2y+a_3xy$) to be a good fit without overparameterization. Due to presence of extreme values in both FNR and HCHO×NO_2, we use a weighted least squares method for the curve fitting based on the distance of the fitted curve to the

data points (known as bi-squares weighting). The best fit with R^2 equals to 0.94 and an RMSE of 0.60 ppbv/hr is:

$$PO_3 = 0.74 - 0.09\,x - 0.02\,y + 0.25xy \quad (4)$$

where x and y are FNR (unitless) and HCHO×NO_2 (ppbv^2), respectively. The residual of the fit is shown in Figure S11. The gradients of PO_3 with respect to x and y are:

$$\frac{dPO_3}{dx} = 0.25y - 0.09 \quad (5)$$

$$\frac{dPO_3}{dy} = 0.25x - 0.02 \quad (6)$$

An apparent observation arises from these equations that is the derivatives of PO_3 to each metric depends on the other one underscoring their interconnectedness. For instance, Eq. (6) suggests that larger FNRs (x) result in a larger gradient of PO_3 to the abundance of HCHO×NO_2 (y). In very low FNRs, this gradient can become very small rendering PO_3 insensitive (or in extreme cases, negatively correlated) to HCHO×NO_2. This analysis provides encouraging results about the future application of the satellite-derived HCHO×NO_2; however, the wide class of problems relating to the application of satellite-derived FNR columns such as satellite errors in columns or the translation between columns to PBL are also present in Eq. (4), even in a more pronounced way due to HCHO×NO_2 and $HCHO^2$ (= xy). This new perspective into PO_3 estimation deserves a separate study.

3.5. Altitude dependency and its parametrization

A lingering concern over the application of satellite-based FNR tropospheric columns is that the vertical distribution of HCHO and NO_2 are integrated in columns thus this vertical information is permanently lost. As such, here we provide insights on the vertical distribution of FNR within the tropospheric column. This task requires information about the differences between i) the vertical shape of HCHO and that of NO_2 and ii) the vertical shape in the sensitivity of the retrievals to the different altitude layers (described as scattering weights). Ideally, if both compounds show an identically relative shape, the FNR columns will be valid for every air parcel along the vertical path (i.e., a straight line). Previous studies such as Jin et al. (2017) and Schroeder et al. (2017) observed a large degree of vertical inhomogeneity in both HCHO and NO_2 concentrations suggesting that this ideal condition cannot be met. We do not always know the precise knowledge of HCHO and NO_2 vertical distributions, but we can constitute some degree of generalizations by leveraging the measurements made during the aircraft campaigns. As for the differences in the vertical shapes (i.e., the curvature) of the sensitivity of the retrievals between HCHO and NO_2 channels (i.e., ~ 340 nm and ~440 nm), under normal atmospheric and viewing geometry conditions, several studies such as Nowlan et al. 2018 and Lorente et al. 2017 showed small differences in the vertical shapes of the scattering weights within first few kilometers altitude above the surface where the significant fluctuations in FNRs usually take place. Therefore, we do not consider the varying vertical shapes in the scattering weights in our analysis. This assumption might not hold for excessive aerosol loading with variable extinction efficiency between ~340 nm and ~440 nm wavelengths or extreme solar zenith angles.

Figure 5 demonstrates the violin plot of the afternoon (> 12:00 LST) vertical distribution of HCHO, NO_2, and FNR observed by NASA's aircrafts during the four field campaigns analyzed in this study superimposed by the simulated PO_3 rates. The vertical layers are grouped into sixteen altitudes ranging from 0.25 km to 7.75 km. Each vertical layer incorporates measurements ±0.25 km of the altitude mid-layer height. The observations do not follow a normal distribution,

particularly in the lower parts of the atmosphere; thus medians are preferred to represent the central tendency. While the largest PO_3 rates tend to occur in areas close to the surface (< 2 km agl), a nonnegligible fraction of the elevated PO_3 rates are also observed in other parts of the atmosphere such as ~~those in~~ the free troposphere.

Several intriguing features are observed from Figure 5: First, up to the 5.75 km range, which encompasses the PBL area and a large portion of the free-troposphere, NO_2 concentrations tend to decrease quicker than those of HCHO in line with previous studies such as Schroeder et al. (2017), Jin et al. (2017), Chan et al. (2019), and Ren et al. (2022). Second, above 5.75 km, HCHO levels off whereas NO_2 shows an increasing trend. As a result of their different vertical trends, we observe nonuniformities in the vertical distribution of FNR: they become more NOx-sensitive with altitude up to a turning point at 5.75 km and then shift backwards to VOC-sensitive.

It is attractive to model these shapes and apply parameterizations to understand how their shapes will complicate the use of tropospheric column retrieval from satellites. First order rational functions are a good candidate to use. Concerning the vertical dependency of HCHO and NO_2, we find reasonable fit (R^2=0.73) as:

$$HCHO, NO_2 = \frac{a_0 z + a_1}{z + a_2} \tag{7}$$

where z is altitude in km. a_i (i=0,1,2) are fitting parameters. From this equation it is determined that FNRs follow a second order rational function:

$$f(z) = \frac{HCHO}{NO_2} = \frac{b_0 z^2 + b_1 z + b_2}{b_3 z^2 + b_4 z + b_5} \tag{8}$$

where b_i (i=0, … , 5) are fitting parameters. One can effortlessly fit this function to different bounds of the vertical distribution of FNR such as the 25th and 75th percentiles, and subsequently estimate the first moment of the resultant polygon along z divided by the total area bounded to the polygon (the centroid, G) via:

$$G(z_1, z_2) = \frac{1}{2A} \int_{z1}^{z2} f^2(z)_{75th} - f^2(z)_{25th}\, dz \tag{9}$$

where A is the area of the polygon bounded by the 75th percentiles, $f(z)_{75th}$, and the 25th percentiles ($f(z)_{25th}$) of FNR (shown in Figure 5 as solid black lines). We define an altitude adjustment factor (f_{adj}) such that one can translate an observed FNR tropospheric column ratio~~s~~, such as those retrieved from satellites, to a defined altitude and below that point (zt) through:

$$f_{\text{adj}} = \frac{G(0, z_t)}{G(0{,}8\ km)} \tag{10}$$

where zt can be interchanged to match the PBLH. This definition is more beneficial than using the entire tropospheric column to the surface conversion (e.g., Jin et al., 2017) because ozone can be formed in various vertical layers. Using the observations collected during the campaign, we estimate Eq. (10) along with ±1σ boundaries shown in Figure 6. To determine the adjustment factor error, we reestimate Eq.9 with ±1σ level in the coefficients obtained from Eq.8. The resultant error is shown in the dashed red line in Figure 6. This error results from uncertainties associated with assuming that the second-order rational function can explain the vertical distribution of FNRs. The shape of the resulting adjustment factor is in line with of the vertical distribution of FNR (see Figure 5): the adjustment factor curve closer to the surface has values smaller than one, increases to values larger than one in the mid-troposphere, and finally converges to one near the top of the tropospheric column. If one picks out an altitude pertaining to a PBLH, they can easily apply f_{adj} to the observed FNR columns to estimate the corresponding ratio for that specific PBLH. A more

evolved PBLH (i.e., a large *zt*) results in stronger vertical mixing rendering f_{adj} closer to one. The standard error deviation of this conversion is around 26%.

It is beneficial to model this curve to make this data-driven conversion easier for future applications. A second-order polynomial can well describe (R^2=0.99) this curve:

$$f_{\text{adj}} = az_t^2 + bz_t + c \qquad a = -0.02, b = 0.25, c = 0.41 \qquad (11)$$

Although Eq. (11) does not include observations above 8 km, the area bounded between $f(z)_{75th}$ and $f(z)_{25th}$ in higher altitudes is too small to make a noticeable impact on this adjustment factor.

One may object that since we estimated the adjustment factor based on two boundaries (25th and 75th percentiles) of the data we are no longer really dealing with 50% of features observed in the vertical shapes of FNR. This valid critique can be overcome by gradually relaxing the lower and upper limits and examine the resulting change in f_{adj}. When we reduce the lower limit in Eq. (9) from the 25th to 1st percentiles the optimal curve is similar to the one shown in Figure 6 (Figure S12). However, when we extend the upper limit from 75th percentiles to greater values, we see the fit becoming less robust above the 80th percentiles indicating that the formulation is applicable for ~80% of the data. The reason behind the poor representation of the adjustment factor for the upper tail of the population is the extremely steep turning point between 5.5 and 6.0 km necessitating a higher order rational function to be used for Eq. (7) and Eq. (8). We prefer to limit this analysis to both boundaries and the order defined in Eq. (8) and Eq. (9) because extreme value predictions usually lack robustness.

A caution with these results is that our analysis is limited to afternoon observations because our focus is on afternoon low orbiting sensors such as OMI and TROPOMI. Nonetheless, Schroeder et al. (2017) and Crawford et al. (2021) observed a large diurnal variability in these profiles due to diurnal variability in sinks and sources of NO_2 and HCHO, and atmospheric dynamics. The diurnal cycle has indeed an important implication for geostationary satellites such as Tropospheric Emissions: Monitoring of Pollution (TEMPO) (Chance et al., 2019).

Another important caveat with our analysis is that it is based upon four air quality campaigns taking place in warm seasons avoiding times/areas with convective transport; as such our analysis is ignorant about the vertical shapes of FNR during convective activities and cold seasons. These oversights can be downplayed by a few compelling assumptions: first, it is very atypical to encounter elevated ozone production rates during cold seasons with few exceptions (Ahmadov et al., 2015; Rappenglück et al., 2014); second, the notion of ozone regimes is only appropriate in photochemically active environments where the ROx-HOx cycle is active; an example of this can be found in Souri et al. (2021) who observed an enhancement of surface ozone in central Europe during a lockdown in April 2020 (up to 5 ppbv) compared to a baseline which was explainable by the reduced O_3 titration through NO in place of the photochemically induced production. An exaggerated extension to this example is the nighttime chemistry where NO-O_3-NO_2 partitioning is the major driver of negative ozone production rates; at night, the definition of NOx-sensitive or VOC-sensitive is meaningless, so is in photochemically less active environments; third, it is rarely advisable to use cloudy scenes in satellite UV-Vis gas retrievals due to the arguable assumption on Lambertian clouds and highly uncertain cloud optical centroid and albedo; accordingly, convection occurring during storms or fires are commonly masked in satellite-based studies. Therefore, the limitations associated with the adjustment factor are mild compared to the advantages.

3.6. *Spatial Heterogeneity*

The spatial representation error resulting from both unresolved processes and scales (Janić et al., 2016; Valin et al., 2011; Souri et al., 2022) refers to the amount of information lost due to satellite footprint or unresolved inputs used in satellite retrieval algorithms. This source of error cannot be determined when we do not know the true state of the spatial variability. There is, however, a practical way to determine this by conducting multi-scale intercomparisons of a coarse spatial resolution output against a finer one. Yet, despite the absence of the truth in this approach, we tend to find their comparisons useful in giving us an appreciation of the error.

We build the reference data on qualified pixels (qa_value> 0.75) of offline TROPOMI tropospheric NO_2 version 2.2.0 (van Geffen et al., 2021; Boersma et al., 2018) and total HCHO columns version 2.02.01 (De Smedt et al., 2018) oversampled at 3×3 km^2 in summer 2021 over the US. Figure 7 shows the map of those tropospheric columns as well as FNR. Encouragingly, the small footprint and relatively low detection limit of TROPOMI compared to its predecessor satellite sensors (e.g., OMI) enables us to have possibly one of the finest maps of HCHO over the US to date. Large values of HCHO columns are found in the southeast due to strong isoprene emissions (e.g., Zhu et al., 2016; Wells et al., 2020). Cities like Houston (Boeke et al., 2011; Zhu et al., 2014; Pan et al., 2015; Diao et al., 2016), Kansas City, Phoenix (Nunnermacker et al., 2004), and Los Angeles (de Gouw et al., 2018) also show pronounced enhancements of HCHO possibly due to anthropogenic sources. Expectedly, large tropospheric NO_2 columns are often confined to cities and some coal-fired power plants along Ohio river basin. Concerning FNR, low values dominate cities whereas high values are found in remote regions. An immediate tendency observed from these maps is that the length scale of HCHO columns is longer than that of NO_2. This indicates that NO_2 columns are more heterogenous. It is because of this reason that we observe a large degree of the spatial heterogeneity with respect to FNRs.

Here we limit our analysis to Los Angeles due to computational costs imposed by the subsequent experiment. To quantify the spatial representation errors caused by satellite footprint size, we upscale the FNRs by convolving the values with four low pass box filters with the size of 13×24, 36×36, 108×108, and 216×216 km^2, shown in the first column of Figure 8. Subsequently, to extract the spatial variance (information), we follow the definition of the experimental semivariogram (Matheron, 1963):

$$\gamma(\boldsymbol{h}) = \frac{1}{2N(\boldsymbol{h})} \sum_{|x_i - x_j| - |\boldsymbol{h}| \le \varepsilon} [Z(x_i) - Z(x_j)]^2 \quad (12)$$

where $Z(x_i)$ (and $Z(x_j)$) is discrete pixels of FNRs, $N(\boldsymbol{h})$ is the number of paired pixels separated by the vector of $\boldsymbol{h}$. The |.| operator indicates the length of a vector. The condition of $|x_i - x_j| - |\boldsymbol{h}| \le \varepsilon$ is to permit certain tolerance for differences in the length of the vector. Here, we rule out the directional dependency in $\gamma(\boldsymbol{h})$, which in turn, makes the vector of $\boldsymbol{h}$ scalar ($h = |\boldsymbol{h}|$). Moreover, we bin γ values in 100 evenly-spaced intervals ranging from 0 to 5 degree. To remove potential outliers (such as noise), it is wise to model the semivariogram using an empirical regression model. To model the semivariogram, we follow the stable Gaussian function used in Souri et al. (2022):

$$\gamma(h) = s(1 - e^{-(\frac{h}{r})^{c_0}}): c_0 = 1.5 \quad (13)$$

where r and s are fitting parameters. For the most part, geophysical quantities become spatially uncorrelated at a certain distance called the range and the variance associated with that distance is called the sill. The fitting parameters, r and s, describe these two quantities as long as the stable

Gaussian function can well fit to the shape of semivariogram. The semivariograms, and the fits, associated with each map is depicted in the second column of Figure 8.

The modeled semivariograms suggest that a coarser field comes with a smaller sill, implying a loss in the spatial information (variance). The length scale (i.e., the range) only sharply increases at coarser footprints (>36×36 km^2). This indicates that several coarse resolution satellite sensors such as OMI (13×24 km^2) are rather able to determine the length scales of FNR over a major city such as Los Angeles. By leveraging the modeled semivariograms, we can effortlessly determine the spatial representation error for specific scale (e.g., h=10 km) through

$$e^2(h) = 1 - \frac{\gamma(h)}{\gamma_{ref}(h)} \quad (14)$$

where $\gamma(h)$ and $\gamma_{ref}(h)$ is the modeled semivariogram of the target and the reference fields (3×3 km^2). This equation articulates the amount of information lost in the target field for the reference. Accordingly, the proposed formulation of the spatial representation error is relative. For the most part, the OMI nadir pixel (13×24 km^2) only have a ~12% loss of the spatial variance. On the contrary, a grid box with a size of 216×216 km^2 fails at capturing ~65% of the spatial information in FNR with a 50 km length scale comparable to the extent of Los Angeles. The advantage of our method is that we can mathematically describe the spatial representation error as function of the length of our target. The present method can be easily applied to other atmospheric compounds and locations. We have named this method SpaTial Representation Error EstimaTor (STREET) which is publicly available as an open-source package (Souri, 2022).

An oversight in the above experiment lies in its lack of appreciation of unresolved physical processes in the satellite measurements: weaker sensitivity of some spectra windows to the near-surface pollution (Yang et al., 2014), using 1-D air mass factor calculation instead of 3-D (Schwaerzel et al., 2020), and discounting aerosol effect on the light path are just few examples to point out. To account for the unresolved processes, one can recalculate Eqs. (12)-(14) using outputs coming from different retrieval frameworks, which is beyond the scope of this study.

3.7. Satellite errors

3.7.1. Concept

Two types of retrieval errors can affect our analysis: systematic errors (bias) and unsystematic ones (random errors). In theory, it is very compelling to understand their differences. In reality, the distinction between random and systematic errors is not as clear-cut as it seems. One may wish to establish the credibility of a satellite retrieval by comparing it to a sky-radiance measurement over time. Because each measurement is made at a different time, their comparison is not a repetition of the same experiment; each time, the atmosphere differs in some aspects so each comparison is unique. Adding more sky-radiance measurements will simply add new experiments. For each paired data points, there are many unique issues contributing differently to errors; as such our problem is grossly under-determined (i.e., more unknowns for a given observation). Here, we do not attempt to separate those types of errors in the subsequent analysis, thereby limiting the analysis to the total uncertainty.

We focus on analyzing the statistical errors drawn from the differences between benchmark and the retrievals on daily basis. Two sensors are used for this analysis: TROPOMI and OMI. To propagate individual uncertainties in HCHO and NO_2 to FNRs, we follow an analytical approach involving Jacobians of the ratio to HCHO and NO_2. Assuming that errors in HCHO and NO_2 are uncorrelated, the relative error of the ratio can be estimated by:

$$\frac{\sigma}{ratio} = \sqrt{\left(\frac{\sigma_{HCHO}}{HCHO}\right)^2 + \left(\frac{\sigma_{NO_2}}{NO_2}\right)^2} \quad (15)$$

where σ_{HCHO} and σ_{NO_2} are total uncertainties of HCHO and NO_2 observations. It is important to recognize that the errors in HCHO and NO_2 are not strictly uncorrelated due to assumptions made in their air mass factor calculations. The consequence of disregarding the correlated errors is an underestimation in the final error.

3.7.2. Error Distributions in TROPOMI and OMI

We begin our analysis with the error distribution of daily TROPOMI tropospheric NO_2 columns (v1.02.02) against 22 MAX-DOAS instruments from May to Sep in 2018-2021. The data are paired based on the criteria defined in Verhoelst et al. (2021). The spatial locations of the stations are mapped in Figure S13. Figure 10a shows the histogram of the TROPOMI minus the MAX-DOAS instruments. The first observation from this distribution is that it is skewed towards lower differences evident in the skewness parameter around -4.6. As a result of the skewness, the median should be a better representative of the central tendency which is around -1×10^{15} molec./cm^2. In general, TROPOMI tropospheric NO_2 columns show a low bias. We fit a normal distribution to the data using non-linear Levenberg-Marquardt method. This fitted normal distribution (R^2=0.94) is used to approximate σ_{NO_2} for different confidence intervals and to play down blunders. To understand how much of these disagreements are caused by systematic errors as opposed to random errors, we redo the histogram using monthly-based observations (Figure S14). A slight change in the dispersions between the daily and the monthly-basis analysis indicates the significance of unresolved systematic (or relative) biases. This tendency suggests, when conducting the analysis on a monthly basis, the relative bias cannot be mitigated by averaging. Verhoelst et al. (2021) rigorously studied the potential root cause of some discrepancies between MAX-DOAS and TROPOMI. An important source of error stems from the fundamental differences in the vertical sensitivities of MAX-DOAS (more sensitive to the lower tropospheric region) and TROPOMI (more sensitive to the upper tropospheric area). This systematic error can only be mitigated using reliably high-resolution vertical shape factors instead of spatiotemporal averaging of the satellite data.

The error analysis for OMI follows the same methods applied for TROPOMI; however, with different benchmarks. We follow the comparisons made between the operational product version 3.1 and measured columns derived from NCAR's NO_2 measurements integrated along aircraft spirals during four NASA's air quality campaigns. More information regarding this data comparison can be found in Choi et al. (2020). Figure 10b shows the histogram of OMI minus the integrated spirals. Compared to TROPOMI, the OMI bias is worse by a factor of two. The standard deviation calculated from a Gaussian fit (2.31×10^{15} molec./cm^2) is not substantially different than that of TROPOMI (2.11×10^{15} molec./cm^2).

As for the error distribution of TROPOMI HCHO columns (version 1.1.(5-7)), we use 24 FTIR measurements during the same time period based on the criteria specified in Vigouroux et al. (2020). The stations are mapped in Figure S13. The frequency of the paired data is daily. Figure 11a depicts the error distribution. The distribution is slightly broader compared to that of NO_2, manifested in a larger standard deviation 4.32×10^{15} molec./cm^2. This is primarily due to the fact that the molecular absorption of HCHO is much smaller/narrower than that of NO_2 in the UV-Vis range (Gonzalez Abad et al., 2019); consequently, HCHO observations are more contaminated by

noise. Similar to the NO_2, we fit a normal distribution (R^2=0.90) to specify σ_{HCHO} for different confidence intervals.

Concerning OMI HCHO columns from SAO version 3 (Gonzalez Abad et al., 2015), we follow the intercomparison approach proposed in Zhu et al. (2020). Based on this approach, the benchmarks come from GEOS-Chem simulated HCHO columns corrected by in-situ aircraft measurements. The measurements were made during ozone seasons from KORUS-AQ, DISCOVERs, FRAPPE, NOMADSS, and SENEX campaigns (see Table 1 in Zhu et al. 2020). OMI values ranging from -0.5×10^{15} molec./cm^2 and 1.0×10^{17} molec./cm^2 with effective cloud fraction between 0.0 and 0.3, and SZA between 0 and 60 degrees are only considered in the comparison. Any pixels from OMI and grid boxes from the corrected GEOS-Chem simulation that fall into a polygon enclosing the campaign domain are used to create the error distribution shown in Figure 11b. The distribution has much denser data because the model output covers a large portion of the satellite swath. The error distribution suggests that OMI HCHO is inferior to TROPOMI evident in larger bias and standard deviation. The OMI bias is twice as large as that of TROPOMI. De Smedt et al. (2021) observed the same level of bias from their comparisons of OMI/TROPOMI with MAX-DOAS instruments (see Table 3 in their paper). Moreover, their OMI vs MAX-DOAS comparisons were severely scattered. Likewise, we observe the standard deviation of OMI from the fitted Gaussian function to be roughly five times as large of that TROPOMI. This can primarily due to a weaker signal-to-noise (and sensor degradation) in OMI. It is because of this reason that OMI HCHO should be ~~oversampled for few~~ months. Another possible reason for the large standard deviation is the fact that the benchmark arises from a modeling experiment whose ability at resolving spatiotemporal variations in HCHO may be uncertain. This partly leads to the performance of OMI to look poor.

3.7.3. The impact of retrieval error on the ratio

Following Eq. (15), we calculate the standard error for a wide range of NO_2 and HCHO columns at 68% confidence interval (1 sigma) for both TROPOMI and OMI derived from the fitted Gaussian function to the histograms; the standard errors are shown in Figure 12. We observe smaller errors to be associated with larger tropospheric column concentrations. As for TROPOMI, either daily HCHO or tropospheric NO_2 columns should be above $1.2\text{-}1.5\times10^{16}$ molec./cm^2 to achieve 20-30% standard error. The TROPOMI errors start diminishing the application of FNR when both measurements are below this threshold. Regarding OMI, it is nearly impossible to get the standard error below of 20-30% given its problematically large HCHO standard deviation. For 50% error, the daily HCHO columns should be above 3.2×10^{16} molec./cm^2. This range of error can also be achieved if OMI tropospheric NO_2 columns are above 8×10^{15} molec./cm^2.

3.8. The fractional errors to the combined error

The ultimate task is to compile the aforementioned errors to gauge how each individual source of error contributes to the overall error. Although each error is different in nature, combined they explain the uncertainties of one quantity (FNR) and can be roughly considered independent; therefore, the combined error is given by:

$$\sigma_{total} = \sqrt{\sigma_{Col2PBL}^2 + \sigma_{SpatialRep}^2 + \sigma_{Retreival}^2} \quad (16)$$

$\sigma_{Col2PBL}$ is the error in the adjustment-factor defined in this study. We calculated a 26% standard error for a wide range of PBLHs. Therefore, $\sigma_{Col2PBL}$ equals to 26% of the observed ratio (i.e., magnitude dependent). $\sigma_{SpatialRep}$ is more complex. It is a function of the footprint of the satellite

(or a model), the spatial variability of the reference field which varies from environment to environment, and the length scale of our target (e.g., a district, a city, or a state). Eq. (14) explicitly quantifies this error. The product of the square root of that value and the observed ratio defines $\sigma_{SpatialRep}$. The last error depends on the magnitude of HCHO and NO_2 tropospheric columns. It can be estimated from Eq. (15) times the observed ratio. We did not include the chemistry error in Eq. (16) because it was suited only for segregating the chemical conditions; it does not describe the level of uncertainties that comes with the observed columnar ratio. Figure 13 shows the total relative error given the observed TROPOMI ratio seen in Figure 7. We consider the OMI spatial representation error (13% variance loss) for this case that was computed in a city environment. The retrieval errors are based on TROPOMI sigma values. Areas associated with relatively small errors (<50%) are mostly seen in cities due to a stronger signal (smaller $\sigma_{Retreival}$). Places with low vegetation and anthropogenic sources (i.e., Rocky Mountains) possess the largest errors (>100%).

To produce some examples of the fractional errors to the combined error, we focus on two different environments with two different sets of HCHO and NO_2 columns. One represents a heavily polluted area, and the other one a moderately polluted region. We also include two footprints: OMI (13×24 km^2) and a 108×108 km^2 pixel. Finally, we calculate the percentage of each error component for both OMI and TROPOMI sensors. Figure 14 shows the pie charts describing the percentage of each individual error to the total error for TROPOMI. Unless the footprint of the sensor is coarse enough (e.g., 108 km^2) to give rise to the spatial representation error dominance, the retrieval error stands out. It is not expected for new satellites to have very large footprints; as such, the retrieval errors appear to be the major obstacle for using FNR in a robust manner. Figure 15 shows the same calculation but using OMI errors; the retrieval errors massively surpass other errors. This motivates us to do one more experiment; we recalculate the HCHO error distribution in OMI using monthly-averaged data instead of daily (Figure S15). This experiment suggests a standard deviation of 9.4 $\times 10^{15}$ molec./cm^2 with which we again observe the retrieval error to be the largest contributor (>80%) of the combined error (Figure S16). A recent study (Johnson et al., 2022) also suggests that retrieval errors can result in considerable disagreement between FNRs from various sensors and retrieval frameworks.

4. Summary

The main goal of this study was to characterize the errors associated with the ratio of satellite-based HCHO to NO_2 columns which has been widely used for ozone sensitivity studies. From the realization of the complexity of the problem we now know that four major errors should be carefully quantified so that we can reliably represent the underlying ozone regimes. The errors are broken down into i) the chemistry error, ii) the column to the PBL translation, iii) the spatial representation error, and iv) the retrieval error. Each error has its own dynamics and has been tackled differently by leveraging a broad spectrum of tools and data.

The chemistry error refers to the predictive power of $HCHO/NO_2$ ratio (hereafter FNR) at describing the HOx-ROx cycle which can be well explained by the ratio of the chemical loss of HO_2+RO_2 (LROx) to the chemical loss of NOx (LNOx). Because those chemical reactions are not directly observable, we set up a chemical box model constrained with a large suite of in-situ aircraft measurements collected during DISCOVER-AQs and KORUS-AQ campaigns (~ 500 hr of flight). Our box model showed a reasonable performance at recreating some of unconstrained key compounds such as OH (R^2=0.64, bias=17%), HO_2 (R^2=0.66, bias<1%), and HCHO (R^2=0.73). Subsequently we compared the simulated FNRs to LROx/LNOx. They showed a high degree of

correspondence (R^2=0.93) but only in the log-log scale; this indicated that FNRs poorly described the HOx-ROx cycle for heavily polluted environments as well as pristine ones. Following a robust baseline indicator (ln(LROx/LNOx) = -1.0 ± 0.2) segregating NOx-sensitive from VOC-sensitive regimes, we observed a diverse range of FNR ranging from 1 to 4. These transitioning ratios had a Gaussian distribution with a mean of 1.8 and standard deviation of 0.4. This implied that the relative standard error associated with the ratio from the chemistry perspective at 68% confidence interval was 20%. Although this threshold with its error was based on a single model realization and can be different for a different chemical mechanism, it provided a useful universal baseline derived from various chemical and meteorological conditions. At 68% confidence level, any uncertainty beyond 20% in the ozone regime identification from FNRs likely originates from other sources of error such as the retrieval error.

Results from the box model showed that ozone production rates in extremely polluted regions (VOC-sensitive) were not significantly different than those in pristine ones (NOx-sensitive) due to non-linear chemical feedback mostly imposed by NO_2+OH. Indeed, the largest PO_3 rates (median = 4.6 ppbv/hr) were predominantly seen in VOC-sensitive regimes tending towards the transitional regime. This was primary caused by the abundance of ozone precursors (i.e., HCHO×NO_2) in addition to the diminished negative chemical feedback. We also revealed that HCHO×NO_2 can be used as a sensible proxy for the ozone precursors abundance. In theory, this metric in conjunction with the ratio provided reasonable estimates on PO_3 rates (RMSE = ±0.60 ppbv/hr).

We then analyzed the afternoon vertical distribution of HCHO, NO_2, and their ratio observed from aircrafts during the air quality campaigns binned to the near surface to 8 km. For altitudes below 5.75 km, HCHO concentration steadily decreased with altitude but at a smaller rate compared to NO_2. Above that altitude, NO_2 concentrations stabilized and slightly increased due to lightning and stratospheric sources. The dissimilarity between the vertical shape of NO_2 versus HCHO resulted in a non-linear shape of FNR. This non-linear shape necessitated a mathematical formulation to transform an observed columnar ratio to a ratio at a desired vertical height expanding from the surface. We fit a second-order rational function to the profile and formulated the altitude adjustment factor which clearly followed a second-order polynomial function starting from values below 1 for lower altitudes, following values above 1 for some high altitudes, and finally converging to 1 at 8 km. This behavior means that for a given tropospheric columnar ratio, the ozone regime tends to get pushed towards the VOC-sensitive regime near the surface. This data-driven adjustment factor exclusively derived from afternoon aircraft profiles during warm seasons in non-convective conditions had a standard error of 26%.

An important error in the satellite-based observations stemmed from unresolved spatial variability in trace gas concentrations within a satellite pixel (Souri et al., 2022; Tang et al., 2021). The amount of unresolved spatial variability (the spatial representation error) can in principle be modeled if we base our reference on a distribution map made from a high spatial resolution dataset. We modeled semivariograms (or spatial auto-correlation) computed for a reference map of FNR observed by TROPOMI at 3×3 km^2 over Los Angeles. Subsequently, we coarsened the map to 13×24, 36×36, 108×108, and 216×216 km^2 and modeled their semivariograms. As for 13×24 km^2, which is equivalent of the OMI nadir spatial resolution, around 12% of spatial information (variance) was lost due to its footprint. The larger the footprint, the bigger spatial representation error. For instance, a grid box with the size of 216×216 km^2 lost 65% of the spatial information in the ratio at 50 km length scale. Our method is compelling to understand and easy to apply for other

products and different atmospheric environments. We developed an open-source package called SpaTial Representation Error EstimaTor (STREET) (Souri, 2022) based on this approach.

We presented estimates of retrieval errors associated with daily TROPOMI and OMI tropospheric NO_2 columns by comparing them against a large suite of MAX-DOAS (Verhoelst et al. 2021) and vertically-integrated measurements from aircraft spirals (Choi et al., 2020). Both products were smaller than the benchmark. Furthermore, they show a relatively consistent dispersion at 68% confidence level (~2×10^{15} molec./cm^2) suggested by fitting a normal function (R^2>0.9) to their error distributions. As for daily TROPOMI and OMI HCHO products, we used global FTIR observations (Vigouroux et al., 2020) and data-constrained GEOS-Chem outputs from multiple campaigns (Zhu et al., 2020), respectively. TROPOMI HCHO indeed outperforms OMI HCHO with respect to bias and dispersion on a daily basis. The standard deviation of OMI HCHO was found to be roughly five times as large compared to TROPOMI. While this error can be partly reduced by oversampling over a span of a month or a season, it is critical to recognize that ozone events are episodic, thus daily observations should be the standard mean for understanding the chemical pathways for the formation of tropospheric ozone. After combining the daily biases from both HCHO and NO_2 TROPOMI comparisons, we came to the conclusion that either daily HCHO or tropospheric NO_2 columns should be above 1.2-1.5$\times10^{16}$ molec./cm^2 to achieve 20-30% standard error in the ratio. Due to the large error in daily OMI HCHO, it was nearly impossible to achieve 20-30% standard error given the observable range of HCHO and NO_2 columns over our planet. To reach to 50% error using daily OMI data, either HCHO columns should be above 3.2×10^{16} molec./cm^2 or tropospheric NO_2 columns should be above 8×10^{15} molec./cm^2.

To build intuition in the significance of the errors above, we finally calculated the combined error in the ratio by linearly combining the root sum of the squares of the TROPOMI retrieval errors, the spatial representation error pertaining to OMI nadir footprint over a city-like environment, and the altitude adjustment error for a wide range of observed HCHO and NO_2 columns over the US. These observations were based on the TROPOMI in summertime 2021. The total errors were relatively mild (<50%) in cities due to a stronger signal, whereas they easily exceeded 100% in regions with low vegetation and anthropogenic sources (i.e., Rocky Mountains). The dominant source of the combined error (40-90%) was the retrieval error.

All of these aspects highlight the necessity of improving the trace gas satellite retrieval algorithms in conjunction with sensor calibration, although with the realization that a better retrieval is somewhat limited by the advancements made in other disciplines such as atmospheric modeling and molecular spectroscopy.

Acknowledgment

This study was funded by NASA's Aura Science Team (grant number: 80NSSC21K1333). PTR-MS measurements were supported by the Austrian Federal Ministry for Transport, Innovation and Technology (bmvit, FFG-ALR-ASAP). The PTR-MS instrument team (P. Eichler, L. Kaser, T. Mikoviny, M. Müller) is acknowledged for their support with field work and data processing. We acknowledge FTIR HCHO measurements team including T. Blumenstock, M. De Mazière, M. Grutter, J. W. Hannigan, N. Jones, R. Kivi, E. Lutsch, E. Mahieu, M. Makarova, I. Morino, I. Murata, T. Nagahama, J. Notholt, I. Ortega, M. Palm, A. Röhling, M. Schneider, D. Smale, W. Stremme, K. Strong, Y. Sun, R. Sussmann, Y. Té, and P. Wang. The measurements at Paramaribo have been supported by the BMBF (German Ministry of Education and Research) in the project ROMIC-II subproject TroStra (01LG1904A). The NDACC FTIR stations Bremen, Garmisch, Izaña, Ny-Ålesund, Paramaribo and Karlsruhe have been supported by the German Bundesministerium für Wirtschaft und Energie (BMWi) via DLR under grants 50EE1711A, B and

D. We thank the Meteorological Service Suriname and Cornelis Becker for support. The measurements and data analysis at Bremen are supported by the Senate of Bremen. The NCAR FTS observation programs at Thule, GR, Boulder, CO and Mauna Loa, HI are supported under contract by the National Aeronautics and Space Administration (NASA). The National Center for Atmospheric Research is sponsored by the National Science Foundation. The Thule effort is also supported by the NSF Office of Polar Programs (OPP). Operations at the Rikubetsu and Tsukuba FTIR sites are supported in part by the GOSAT series project. The Paris TCCON site has received funding from Sorbonne Université, the French research center CNRS and the French space agency CNES. The Jungfraujoch FTIR data are primarily available thanks to the support provided by the F.R.S. - FNRS (Brussels), the GAW-CH program of MeteoSwiss (Zürich) and the HFSJG.ch Foundation (Bern). The MAX-DOAS data used in this publication were obtained from A. Bais, J. Burrows, K. Chan, M. Grutter, C. Liu, H. Irie, V. Kumar, Y. Kanaya, A. Piters, C. Rivera-Cárdenas, M. Van Roozendael, R. Ryan, V. Sinha, and T. Wagner. Fast delivery of MAX-DOAS data tailored to the S5P validation was organized through the S5PVT AO project NIDFORVAL. IUP-Bremen ground-based measurements are funded by DLR-Bonn received through project 50EE1709A. We thank the IISER Mohali atmospheric chemistry facility for supporting the MAX-DOAS measurements at Mohali, India. KNMI ground-based measurements in De Bilt and Cabauw are partly supported by the Ruisdael Observatory project, Dutch Research Council (NWO) contract 184.034.015, by the Netherlands Space Office (NSO) for Sentinel-5p/TROPOMI validation, and by ESA via the EU CAMS-27 project. LZ and SS acknowledge grants from Guangdong Basic and Applied Basic Research Foundation (2021A1515110713) and Shenzhen Science and Technology Program (JCYJ20210324104604012). The TROPOMI validation work was supported by BELSPO/ESA through the ProDEx project TROVA-E2 (grant no. PEA 4000116692). TV acknowledges support from BELSPO through BRAIN-BE 2.0 project LEGO-BEL-AQ (contract B2/191/P1/LEGO-BEL-AQ). We thank Glenn Diskin for providing CO, CO_2, and CH_4 measurements. We thank Paul Wennberg for H_2O_2 and HNO_3 measurements.

Data Access

The FTIR and MAXDOAS data used in this publication were partly obtained from the Network for the Detection of Atmospheric Composition Change (NDACC) and are available through the NDACC website www.ndacc.org. The spatial representation error is estimated based on publicly available package, SpaTial Representation Error EstimaTor (STREET) (https://github.com/ahsouri/STREET). DISCOVER-AQ and KORUS-AQ aircraft data can be downloaded from https://www-air.larc.nasa.gov/missions/discover-aq/discover-aq.html and https://www-air.larc.nasa.gov/missions/korus-aq/. TROPOMI NO_2 and HCHO data can be downloaded from https://disc.gsfc.nasa.gov/datasets/S5P_L2__NO2____1/summary and https://disc.gsfc.nasa.gov/datasets/S5P_L2__HCHO___1/summary. The box model results can be obtained by contacting the corresponding author through ahsouri@cfa.harvard.edu.

Author contributions

AHS designed the research, analyzed the data, conducted the simulations, made all figures, and wrote the paper. MSJ, SP, XL, and KC helped with conceptualization, fundraising, and analysis. GMW helped with configuring the box model. AF, AW, WB, DRB, AJW, RCC, KM, and CC measured various compounds during the air quality campaigns. JHC orchestrated all these campaigns and contributed to the model interpretation. TV, SC, and GP provided paired MAX-DOAS and TROPOMI tropospheric NO_2 observations. CV and BL provided paired FTIR and

TROPOMI HCHO observations. SC and LL provided paired integrated aircraft spirals and OMI tropospheric NO_2 observations. LZ and SS provided the paired observations between the corrected GEOS-Chem HCHO and OMI HCHO columns. All authors contributed to the discussion and edited the paper.

References

Ahmadov, R., McKeen, S., Trainer, M., Banta, R., Brewer, A., Brown, S., Edwards, P.M., de Gouw, J.A., Frost, G.J., Gilman, J., Helmig, D., Johnson, B., Karion, A., Koss, A., Langford, A., Lerner, B., Olson, J., Oltmans, S., Peischl, J., Pétron, G., Pichugina, Y., Roberts, J.M., Ryerson, T., Schnell, R., Senff, C., Sweeney, C., Thompson, C., Veres, P.R., Warneke, C., Wild, R., Williams, E.J., Yuan, B., Zamora, R., 2015. Understanding high wintertime ozone pollution events in an oil- and natural gas-producing region of the western US. Atmospheric Chemistry and Physics 15, 411–429. https://doi.org/10.5194/acp-15-411-2015

Bela, M.M., Barth, M.C., Toon, O.B., Fried, A., Ziegler, C., Cummings, K.A., Li, Y., Pickering, K.E., Homeyer, C.R., Morrison, H., Yang, Q., Mecikalski, R.M., Carey, L., Biggerstaff, M.I., Betten, D.P., Alford, A.A., 2018. Effects of Scavenging, Entrainment, and Aqueous Chemistry on Peroxides and Formaldehyde in Deep Convective Outflow Over the Central and Southeast United States. Journal of Geophysical Research: Atmospheres 123, 7594–7614. https://doi.org/10.1029/2018JD028271

Boeke, N.L., Marshall, J.D., Alvarez, S., Chance, K.V., Fried, A., Kurosu, T.P., Rappenglück, B., Richter, D., Walega, J., Weibring, P., Millet, D.B., 2011. Formaldehyde columns from the Ozone Monitoring Instrument: Urban versus background levels and evaluation using aircraft data and a global model. Journal of Geophysical Research: Atmospheres 116. https://doi.org/10.1029/2010JD014870

Boersma, K.F., Eskes, H.J., Brinksma, E.J., 2004. Error analysis for tropospheric NO2 retrieval from space. Journal of Geophysical Research: Atmospheres 109. https://doi.org/10.1029/2003JD003962

Boersma, K.F., Eskes, H.J., Richter, A., De Smedt, I., Lorente, A., Beirle, S., van Geffen, J.H.G.M., Zara, M., Peters, E., Van Roozendael, M., Wagner, T., Maasakkers, J.D., van der A, R.J., Nightingale, J., De Rudder, A., Irie, H., Pinardi, G., Lambert, J.-C., Compernolle, S.C., 2018. Improving algorithms and uncertainty estimates for satellite NO_2 retrievals: results from the quality assurance for the essential climate variables (QA4ECV) project. Atmospheric Measurement Techniques 11, 6651–6678. https://doi.org/10.5194/amt-11-6651-2018

Boersma, K.F., Eskes, H.J., Veefkind, J.P., Brinksma, E.J., van der A, R.J., Sneep, M., van den Oord, G.H.J., Levelt, P.F., Stammes, P., Gleason, J.F., Bucsela, E.J., 2007. Near-real time retrieval of tropospheric NO_2 from OMI. Atmospheric Chemistry and Physics 7, 2103–2118. https://doi.org/10.5194/acp-7-2103-2007

Box, G.E.P., 1976. Science and Statistics. Journal of the American Statistical Association 71, 791–799. https://doi.org/10.1080/01621459.1976.10480949

Brune, W.H., Miller, D.O., Thames, A.B., Brosius, A.L., Barletta, B., Blake, D.R., Blake, N.J., Chen, G., Choi, Y., Crawford, J.H., Digangi, J.P., Diskin, G., Fried, A., Hall, S.R., Hanisco, T.F., Huey, G.L., Hughes, S.C., Kim, M., Meinardi, S., Montzka, D.D., Pusede, S.E., Schroeder, J.R., Teng, A., Tanner, D.J., Ullmann, K., Walega, J., Weinheimer, A., Wisthaler, A., Wennberg, P.O., 2022. Observations of atmospheric oxidation and ozone production in South Korea. Atmospheric Environment 269, 118854. https://doi.org/10.1016/j.atmosenv.2021.118854

Chan, K.L., Wang, Z., Ding, A., Heue, K.-P., Shen, Y., Wang, J., Zhang, F., Shi, Y., Hao, N., Wenig, M., 2019. MAX-DOAS measurements of tropospheric NO_2 and HCHO in Nanjing

and a comparison to ozone monitoring instrument observations. Atmospheric Chemistry and Physics 19, 10051–10071. https://doi.org/10.5194/acp-19-10051-2019

Chance, K., Palmer, P.I., Spurr, R.J.D., Martin, R.V., Kurosu, T.P., Jacob, D.J., 2000. Satellite observations of formaldehyde over North America from GOME. Geophysical Research Letters 27, 3461–3464. https://doi.org/10.1029/2000GL011857

Chance, K., Liu, X., Miller, C.C., Abad, G.G., Huang, G., Nowlan, C., Souri, A., Suleiman, R., Sun, K., Wang, H., Zhu, L., Zoogman, P., Al-Saadi, J., Antuña-Marrero, J.-C., Carr, J., Chatfield, R., Chin, M., Cohen, R., Edwards, D., Fishman, J., Flittner, D., Geddes, J., Grutter, M., Herman, J.R., Jacob, D.J., Janz, S., Joiner, J., Kim, J., Krotkov, N.A., Lefer, B., Martin, R.V., Mayol-Bracero, O.L., Naeger, A., Newchurch, M., Pfister, G.G., Pickering, K., Pierce, R.B., Cárdenas, C.R., Saiz-Lopez, A., Simpson, W., Spinei, E., Spurr, R.J.D., Szykman, J.J., Torres, O., Wang, J., 2019. TEMPO Green Paper: Chemistry, physics, and meteorology experiments with the Tropospheric Emissions: monitoring of pollution instrument, in: Sensors, Systems, and Next-Generation Satellites XXIII. Presented at the Sensors, Systems, and Next-Generation Satellites XXIII, SPIE, pp. 56–67. https://doi.org/10.1117/12.2534883

Chance, K.V., Burrows, J.P., Perner, D., Schneider, W., 1997. Satellite measurements of atmospheric ozone profiles, including tropospheric ozone, from ultraviolet/visible measurements in the nadir geometry: a potential method to retrieve tropospheric ozone. Journal of Quantitative Spectroscopy and Radiative Transfer 57, 467–476. https://doi.org/10.1016/S0022-4073(96)00157-4

Chance, K.V., Burrows, J.P., Schneider, W., 1991. Retrieval and molecule sensitivity studies for the global ozone monitoring experiment and the scanning imaging absorption spectrometer for atmospheric chartography, in: Remote Sensing of Atmospheric Chemistry. Presented at the Remote Sensing of Atmospheric Chemistry, SPIE, pp. 151–165. https://doi.org/10.1117/12.46657

Choi, S., Lamsal, L.N., Follette-Cook, M., Joiner, J., Krotkov, N.A., Swartz, W.H., Pickering, K.E., Loughner, C.P., Appel, W., Pfister, G., Saide, P.E., Cohen, R.C., Weinheimer, A.J., Herman, J.R., 2020. Assessment of NO_2 observations during DISCOVER-AQ and KORUS-AQ field campaigns. Atmospheric Measurement Techniques 13, 2523–2546. https://doi.org/10.5194/amt-13-2523-2020

Choi, Y., Kim, H., Tong, D., Lee, P., 2012b. Summertime weekly cycles of observed and modeled NOx and O3 concentrations as a function of satellite-derived ozone production sensitivity and land use types over the Continental United States. Atmospheric Chemistry and Physics 12, 6291–6307. https://doi.org/10.5194/acp-12-6291-2012

Choi, Y., Souri, A.H., 2015a. Seasonal behavior and long-term trends of tropospheric ozone, its precursors and chemical conditions over Iran: A view from space. Atmospheric Environment 106, 232–240. https://doi.org/10.1016/j.atmosenv.2015.02.012

Choi, Y., Souri, A.H., 2015b. Chemical condition and surface ozone in large cities of Texas during the last decade: Observational evidence from OMI, CAMS, and model analysis. Remote Sensing of Environment 168, 90–101. https://doi.org/10.1016/j.rse.2015.06.026

Crawford, J.H., Ahn, J.-Y., Al-Saadi, J., Chang, L., Emmons, L.K., Kim, J., Lee, G., Park, J.-H., Park, R.J., Woo, J.H., Song, C.-K., Hong, J.-H., Hong, Y.-D., Lefer, B.L., Lee, M., Lee, T., Kim, S., Min, K.-E., Yum, S.S., Shin, H.J., Kim, Y.-W., Choi, J.-S., Park, J.-S., Szykman, J.J., Long, R.W., Jordan, C.E., Simpson, I.J., Fried, A., Dibb, J.E., Cho, S., Kim, Y.P., 2021.

The Korea–United States Air Quality (KORUS-AQ) field study. Elementa: Science of the Anthropocene 9, 00163. https://doi.org/10.1525/elementa.2020.00163

de Gouw, J.A., Gilman, J.B., Kim, S.-W., Alvarez, S.L., Dusanter, S., Graus, M., Griffith, S.M., Isaacman-VanWertz, G., Kuster, W.C., Lefer, B.L., Lerner, B.M., McDonald, B.C., Rappenglück, B., Roberts, J.M., Stevens, P.S., Stutz, J., Thalman, R., Veres, P.R., Volkamer, R., Warneke, C., Washenfelder, R.A., Young, C.J., 2018. Chemistry of Volatile Organic Compounds in the Los Angeles Basin: Formation of Oxygenated Compounds and Determination of Emission Ratios. Journal of Geophysical Research: Atmospheres 123, 2298–2319. https://doi.org/10.1002/2017JD027976

De Smedt, I., Müller, J.-F., Stavrakou, T., van der A, R., Eskes, H., Van Roozendael, M., 2008. Twelve years of global observations of formaldehyde in the troposphere using GOME and SCIAMACHY sensors. Atmospheric Chemistry and Physics 8, 4947–4963. https://doi.org/10.5194/acp-8-4947-2008

De Smedt, I., Pinardi, G., Vigouroux, C., Compernolle, S., Bais, A., Benavent, N., Boersma, F., Chan, K.-L., Donner, S., Eichmann, K.-U., Hedelt, P., Hendrick, F., Irie, H., Kumar, V., Lambert, J.-C., Langerock, B., Lerot, C., Liu, C., Loyola, D., Piters, A., Richter, A., Rivera Cárdenas, C., Romahn, F., Ryan, R.G., Sinha, V., Theys, N., Vlietinck, J., Wagner, T., Wang, T., Yu, H., Van Roozendael, M., 2021. Comparative assessment of TROPOMI and OMI formaldehyde observations and validation against MAX-DOAS network column measurements. Atmospheric Chemistry and Physics 21, 12561–12593. https://doi.org/10.5194/acp-21-12561-2021

De Smedt, I., Stavrakou, T., Hendrick, F., Danckaert, T., Vlemmix, T., Pinardi, G., Theys, N., Lerot, C., Gielen, C., Vigouroux, C., Hermans, C., Fayt, C., Veefkind, P., Müller, J.-F., Van Roozendael, M., 2015. Diurnal, seasonal and long-term variations of global formaldehyde columns inferred from combined OMI and GOME-2 observations. Atmospheric Chemistry and Physics 15, 12519–12545. https://doi.org/10.5194/acp-15-12519-2015

De Smedt, I., Stavrakou, T., Müller, J.-F., van der A, R.J., Van Roozendael, M., 2010. Trend detection in satellite observations of formaldehyde tropospheric columns. Geophysical Research Letters 37. https://doi.org/10.1029/2010GL044245

De Smedt, I., Theys, N., Yu, H., Danckaert, T., Lerot, C., Compernolle, S., Van Roozendael, M., Richter, A., Hilboll, A., Peters, E., Pedergnana, M., Loyola, D., Beirle, S., Wagner, T., Eskes, H., van Geffen, J., Boersma, K.F., Veefkind, P., 2018. Algorithm theoretical baseline for formaldehyde retrievals from S5P TROPOMI and from the QA4ECV project. Atmospheric Measurement Techniques 11, 2395–2426. https://doi.org/10.5194/amt-11-2395-2018

Diao, L., Choi, Y., Czader, B., Li, X., Pan, S., Roy, A., Souri, A.H., Estes, M., Jeon, W., 2016. Discrepancies between modeled and observed nocturnal isoprene in an urban environment and the possible causes: A case study in Houston. Atmospheric Research 181, 257–264. https://doi.org/10.1016/j.atmosres.2016.07.009

Duncan, B.N., Yoshida, Y., Olson, J.R., Sillman, S., Martin, R.V., Lamsal, L., Hu, Y., Pickering, K.E., Retscher, C., Allen, D.J., Crawford, J.H., 2010. Application of OMI observations to a space-based indicator of NOx and VOC controls on surface ozone formation. Atmospheric Environment 44, 2213–2223. https://doi.org/10.1016/j.atmosenv.2010.03.010

Fried, A., Walega, J., Weibring, P., Richter, D., Simpson, I.J., Blake, D.R., Blake, N.J., Meinardi, S., Barletta, B., Hughes, S.C., Crawford, J.H., Diskin, G., Barrick, J., Hair, J., Fenn, M., Wisthaler, A., Mikoviny, T., Woo, J.-H., Park, M., Kim, Jinseok, Min, K.-E., Jeong, S.,

Wennberg, P.O., Kim, M.J., Crounse, J.D., Teng, A.P., Bennett, R., Yang-Martin, M., Shook, M.A., Huey, G., Tanner, D., Knote, C., Kim, JongHo, Park, R., Brune, W., 2020. Airborne formaldehyde and volatile organic compound measurements over the Daesan petrochemical complex on Korea's northwest coast during the Korea-United States Air Quality study: Estimation of emission fluxes and effects on air quality. Elementa: Science of the Anthropocene 8, 121. https://doi.org/10.1525/elementa.2020.121

González Abad, G., Liu, X., Chance, K., Wang, H., Kurosu, T.P., Suleiman, R., 2015. Updated Smithsonian Astrophysical Observatory Ozone Monitoring Instrument (SAO OMI) formaldehyde retrieval. Atmospheric Measurement Techniques 8, 19–32. https://doi.org/10.5194/amt-8-19-2015

Gonzalez Abad, G., Souri, A.H., Bak, J., Chance, K., Flynn, L.E., Krotkov, N.A., Lamsal, L., Li, C., Liu, X., Miller, C.C., Nowlan, C.R., Suleiman, R., Wang, H., 2019. Five decades observing Earth's atmospheric trace gases using ultraviolet and visible backscatter solar radiation from space. Journal of Quantitative Spectroscopy and Radiative Transfer 238, 106478. https://doi.org/10.1016/j.jqsrt.2019.04.030

Janjić, T., Bormann, N., Bocquet, M., Carton, J.A., Cohn, S.E., Dance, S.L., Losa, S.N., Nichols, N.K., Potthast, R., Waller, J.A., Weston, P., 2018. On the representation error in data assimilation. Quarterly Journal of the Royal Meteorological Society 144, 1257–1278. https://doi.org/10.1002/qj.3130

Jeon, W., Choi, Y., Souri, A.H., Roy, A., Diao, L., Pan, S., Lee, H.W., Lee, S.-H., 2018. Identification of chemical fingerprints in long-range transport of burning induced upper tropospheric ozone from Colorado to the North Atlantic Ocean. Science of The Total Environment 613–614, 820–828. https://doi.org/10.1016/j.scitotenv.2017.09.177

Jin, X., Fiore, A.M., Murray, L.T., Valin, L.C., Lamsal, L.N., Duncan, B., Folkert Boersma, K., De Smedt, I., Abad, G.G., Chance, K., Tonnesen, G.S., 2017. Evaluating a Space-Based Indicator of Surface Ozone-NOx-VOC Sensitivity Over Midlatitude Source Regions and Application to Decadal Trends. Journal of Geophysical Research: Atmospheres 122, 10,439-10,461. https://doi.org/10.1002/2017JD026720

Jin, X., Holloway, T., 2015. Spatial and temporal variability of ozone sensitivity over China observed from the Ozone Monitoring Instrument. Journal of Geophysical Research: Atmospheres 120, 7229–7246. https://doi.org/10.1002/2015JD023250

Kleinman, L.I., Daum, P.H., Lee, Y.-N., Nunnermacker, L.J., Springston, S.R., Weinstein-Lloyd, J., Rudolph, J., 2001. Sensitivity of ozone production rate to ozone precursors. Geophysical Research Letters 28, 2903–2906. https://doi.org/10.1029/2000GL012597

Laughner, J.L., Zhu, Q., Cohen, R.C., 2019. Evaluation of version 3.0B of the BEHR OMI NO2 product. Atmospheric Measurement Techniques 12, 129–146. https://doi.org/10.5194/amt-12-129-2019

Lee, H.-J., Chang, L.-S., Jaffe, D.A., Bak, J., Liu, X., Abad, G.G., Jo, H.-Y., Jo, Y.-J., Lee, J.-B., Yang, G.-H., Kim, J.-M., Kim, C.-H., 2022. Satellite-Based Diagnosis and Numerical Verification of Ozone Formation Regimes over Nine Megacities in East Asia. Remote Sensing 14, 1285. https://doi.org/10.3390/rs14051285

Lee, Y., Huey, L.G., Wang, Y., Qu, H., Zhang, R., Ji, Y., Tanner, D.J., Wang, X., Tang, J., Song, W., Hu, W., Zhang, Y., 2021. Photochemistry of Volatile Organic Compounds in the Yellow River Delta, China: Formation of O3 and Peroxyacyl Nitrates. Journal of Geophysical Research: Atmospheres 126, e2021JD035296. https://doi.org/10.1029/2021JD035296

Lorente, A., Folkert Boersma, K., Yu, H., Dörner, S., Hilboll, A., Richter, A., Liu, M., Lamsal, L.N., Barkley, M., De Smedt, I., Van Roozendael, M., Wang, Y., Wagner, T., Beirle, S., Lin, J.-T., Krotkov, N., Stammes, P., Wang, P., Eskes, H.J., Krol, M., 2017. Structural uncertainty in air mass factor calculation for NO_2 and HCHO satellite retrievals. Atmospheric Measurement Techniques 10, 759–782. https://doi.org/10.5194/amt-10-759-2017

Martin, R.V., Chance, K., Jacob, D.J., Kurosu, T.P., Spurr, R.J.D., Bucsela, E., Gleason, J.F., Palmer, P.I., Bey, I., Fiore, A.M., Li, Q., Yantosca, R.M., Koelemeijer, R.B.A., 2002. An improved retrieval of tropospheric nitrogen dioxide from GOME. Journal of Geophysical Research: Atmospheres 107, ACH 9-1-ACH 9-21. https://doi.org/10.1029/2001JD001027

Martin, R.V., Fiore, A.M., Van Donkelaar, A., 2004. Space-based diagnosis of surface ozone sensitivity to anthropogenic emissions. Geophysical Research Letters 31. https://doi.org/10.1029/2004GL019416

Matheron, G., 1963. Principles of geostatistics. Economic Geology 58, 1246–1266. https://doi.org/10.2113/gsecongeo.58.8.1246

Miller, D.O., Brune, W.H., 2022. Investigating the Understanding of Oxidation Chemistry Using 20 Years of Airborne OH and HO2 Observations. Journal of Geophysical Research: Atmospheres 127, e2021JD035368. https://doi.org/10.1029/2021JD035368

Newland, M.J., Bryant, D.J., Dunmore, R.E., Bannan, T.J., Acton, W.J.F., Langford, B., Hopkins, J.R., Squires, F.A., Dixon, W., Drysdale, W.S., Ivatt, P.D., Evans, M.J., Edwards, P.M., Whalley, L.K., Heard, D.E., Slater, E.J., Woodward-Massey, R., Ye, C., Mehra, A., Worrall, S.D., Bacak, A., Coe, H., Percival, C.J., Hewitt, C.N., Lee, J.D., Cui, T., Surratt, J.D., Wang, X., Lewis, A.C., Rickard, A.R., Hamilton, J.F., 2021. Low-NO atmospheric oxidation pathways in a polluted megacity. Atmospheric Chemistry and Physics 21, 1613–1625. https://doi.org/10.5194/acp-21-1613-2021

Nowlan, C.R., Liu, X., Janz, S.J., Kowalewski, M.G., Chance, K., Follette-Cook, M.B., Fried, A., González Abad, G., Herman, J.R., Judd, L.M., Kwon, H.-A., Loughner, C.P., Pickering, K.E., Richter, D., Spinei, E., Walega, J., Weibring, P., Weinheimer, A.J., 2018. Nitrogen dioxide and formaldehyde measurements from the GEOstationary Coastal and Air Pollution Events (GEO-CAPE) Airborne Simulator over Houston, Texas. Atmospheric Measurement Techniques 11, 5941–5964. https://doi.org/10.5194/amt-11-5941-2018

Nunnermacker, L.J., Weinstein-Lloyd, J., Kleinman, L., Daum, P.H., Lee, Y.N., Springston, S.R., Klotz, P., Newman, L., Neuroth, G., Hyde, P., 2004. Ground-based and aircraft measurements of trace gases in Phoenix, Arizona (1998). Atmospheric Environment 38, 4941–4956. https://doi.org/10.1016/j.atmosenv.2004.04.033

Pan, S., Choi, Y., Roy, A., Li, X., Jeon, W., Souri, A.H., 2015. Modeling the uncertainty of several VOC and its impact on simulated VOC and ozone in Houston, Texas. Atmospheric Environment 120, 404–416. https://doi.org/10.1016/j.atmosenv.2015.09.029

Rappenglück, B., Ackermann, L., Alvarez, S., Golovko, J., Buhr, M., Field, R.A., Soltis, J., Montague, D.C., Hauze, B., Adamson, S., Risch, D., Wilkerson, G., Bush, D., Stoeckenius, T., Keslar, C., 2014. Strong wintertime ozone events in the Upper Green River basin, Wyoming. Atmospheric Chemistry and Physics 14, 4909–4934. https://doi.org/10.5194/acp-14-4909-2014

Ren, B., Xie, P., Xu, J., Li, A., Qin, M., Hu, R., Zhang, T., Fan, G., Tian, X., Zhu, W., Hu, Z., Huang, Y., Li, X., Meng, F., Zhang, G., Tong, J., Ren, H., Zheng, J., Zhang, Z., Lv, Y., 2022. Vertical characteristics of NO2 and HCHO, and the ozone formation regimes in

Hefei, China. Science of The Total Environment 823, 153425. https://doi.org/10.1016/j.scitotenv.2022.153425

Schroeder, J.R., Crawford, J.H., Fried, A., Walega, J., Weinheimer, A., Wisthaler, A., Müller, M., Mikoviny, T., Chen, G., Shook, M., Blake, D.R., Tonnesen, G.S., 2017. New insights into the column CH2O/NO2 ratio as an indicator of near-surface ozone sensitivity. Journal of Geophysical Research: Atmospheres 122, 8885–8907. https://doi.org/10.1002/2017JD026781

Schroeder, J.R., Crawford, J.H., Ahn, J.-Y., Chang, L., Fried, A., Walega, J., Weinheimer, A., Montzka, D.D., Hall, S.R., Ullmann, K., Wisthaler, A., Mikoviny, T., Chen, G., Blake, D.R., Blake, N.J., Hughes, S.C., Meinardi, S., Diskin, G., Digangi, J.P., Choi, Y., Pusede, S.E., Huey, G.L., Tanner, D.J., Kim, M., Wennberg, P., 2020. Observation-based modeling of ozone chemistry in the Seoul metropolitan area during the Korea-United States Air Quality Study (KORUS-AQ). Elementa: Science of the Anthropocene 8, 3. https://doi.org/10.1525/elementa.400

Schwaerzel, M., Emde, C., Brunner, D., Morales, R., Wagner, T., Berne, A., Buchmann, B., Kuhlmann, G., 2020. Three-dimensional radiative transfer effects on airborne and ground-based trace gas remote sensing. Atmospheric Measurement Techniques 13, 4277–4293. https://doi.org/10.5194/amt-13-4277-2020

Seinfeld, J. H. and Pandis, S. N., 2006: Atmospheric Chemistry and Physics: From Air Pollution to Climate Change, 2nd Edn., Wiley-Interscience, Hoboken, N.J., ISBN: 978-1-118-94740-1.

Sillman, S., He, D., 2002. Some theoretical results concerning O3-NOx-VOC chemistry and NOx-VOC indicators. Journal of Geophysical Research: Atmospheres 107, ACH 26-1-ACH 26-15. https://doi.org/10.1029/2001JD001123

Sillman, S., Logan, J.A., Wofsy, S.C., 1990. The sensitivity of ozone to nitrogen oxides and hydrocarbons in regional ozone episodes. Journal of Geophysical Research: Atmospheres 95, 1837–1851. https://doi.org/10.1029/JD095iD02p01837

Souri, A.H., Chance, K., Bak, J., Nowlan, C.R., González Abad, G., Jung, Y., Wong, D.C., Mao, J., Liu, X., 2021. Unraveling pathways of elevated ozone induced by the 2020 lockdown in Europe by an observationally constrained regional model using TROPOMI. Atmospheric Chemistry and Physics 21, 18227–18245. https://doi.org/10.5194/acp-21-18227-2021

Souri, A.H., Chance, K., Sun, K., Liu, X., Johnson, M.S., 2022. Dealing with spatial heterogeneity in pointwise-to-gridded- data comparisons. Atmospheric Measurement Techniques 15, 41–59. https://doi.org/10.5194/amt-15-41-2022

Souri, A.H., Nowlan, C.R., Wolfe, G.M., Lamsal, L.N., Chan Miller, C.E., Abad, G.G., Janz, S.J., Fried, A., Blake, D.R., Weinheimer, A.J., Diskin, G.S., Liu, X., Chance, K., 2020. Revisiting the effectiveness of HCHO/NO2 ratios for inferring ozone sensitivity to its precursors using high resolution airborne remote sensing observations in a high ozone episode during the KORUS-AQ campaign. Atmospheric Environment 224, 117341. https://doi.org/10.1016/j.atmosenv.2020.117341

Souri. (2022). ahsouri/STREET: STREET 0.0.2 (0.0.2). Zenodo. https://doi.org/10.5281/zenodo.6993116

Tang, W., Edwards, D.P., Emmons, L.K., Worden, H.M., Judd, L.M., Lamsal, L.N., Al-Saadi, J.A., Janz, S.J., Crawford, J.H., Deeter, M.N., Pfister, G., Buchholz, R.R., Gaubert, B., Nowlan, C.R., 2021. Assessing sub-grid variability within satellite pixels over urban regions

using airborne mapping spectrometer measurements. Atmospheric Measurement Techniques 14, 4639–4655. https://doi.org/10.5194/amt-14-4639-2021

Thornton, J.A., Wooldridge, P.J., Cohen, R.C., Martinez, M., Harder, H., Brune, W.H., Williams, E.J., Roberts, J.M., Fehsenfeld, F.C., Hall, S.R., Shetter, R.E., Wert, B.P., Fried, A., 2002. Ozone production rates as a function of NOx abundances and HOx production rates in the Nashville urban plume. Journal of Geophysical Research: Atmospheres 107, ACH 7-1-ACH 7-17. https://doi.org/10.1029/2001JD000932

Tonnesen, G.S., Dennis, R.L., 2000a. Analysis of radical propagation efficiency to assess ozone sensitivity to hydrocarbons and NO x : 1. Local indicators of instantaneous odd oxygen production sensitivity. Journal of Geophysical Research: Atmospheres 105, 9213–9225. https://doi.org/10.1029/1999JD900371

Tonnesen, G.S., Dennis, R.L., 2000b. Analysis of radical propagation efficiency to assess ozone sensitivity to hydrocarbons and NO x : 2. Long-lived species as indicators of ozone concentration sensitivity. Journal of Geophysical Research: Atmospheres 105, 9227–9241. https://doi.org/10.1029/1999JD900372

Valin, L.C., Russell, A.R., Hudman, R.C., Cohen, R.C., 2011. Effects of model resolution on the interpretation of satellite NO2 observations. Atmospheric Chemistry and Physics 11, 11647–11655. https://doi.org/10.5194/acp-11-11647-2011

van Geffen, J., Eskes, H., Compernolle, S., Pinardi, G., Verhoelst, T., Lambert, J.-C., Sneep, M., ter Linden, M., Ludewig, A., Boersma, K.F., Veefkind, J.P., 2022. Sentinel-5P TROPOMI NO_2 retrieval: impact of version v2.2 improvements and comparisons with OMI and ground-based data. Atmospheric Measurement Techniques 15, 2037–2060. https://doi.org/10.5194/amt-15-2037-2022

Verhoelst, T., Compernolle, S., Pinardi, G., Lambert, J.-C., Eskes, H.J., Eichmann, K.-U., Fjæraa, A.M., Granville, J., Niemeijer, S., Cede, A., Tiefengraber, M., Hendrick, F., Pazmiño, A., Bais, A., Bazureau, A., Boersma, K.F., Bognar, K., Dehn, A., Donner, S., Elokhov, A., Gebetsberger, M., Goutail, F., Grutter de la Mora, M., Gruzdev, A., Gratsea, M., Hansen, G.H., Irie, H., Jepsen, N., Kanaya, Y., Karagkiozidis, D., Kivi, R., Kreher, K., Levelt, P.F., Liu, C., Müller, M., Navarro Comas, M., Piters, A.J.M., Pommereau, J.-P., Portafaix, T., Prados-Roman, C., Puentedura, O., Querel, R., Remmers, J., Richter, A., Rimmer, J., Rivera Cárdenas, C., Saavedra de Miguel, L., Sinyakov, V.P., Stremme, W., Strong, K., Van Roozendael, M., Veefkind, J.P., Wagner, T., Wittrock, F., Yela González, M., Zehner, C., 2021. Ground-based validation of the Copernicus Sentinel-5P TROPOMI NO_2 measurements with the NDACC ZSL-DOAS, MAX-DOAS and Pandonia global networks. Atmospheric Measurement Techniques 14, 481–510. https://doi.org/10.5194/amt-14-481-2021

Vigouroux, C., Langerock, B., Bauer Aquino, C. A., Blumenstock, T., Cheng, Z., De Mazière, M., De Smedt, I., Grutter, M., Hannigan, J. W., Jones, N., Kivi, R., Loyola, D., Lutsch, E., Mahieu, E., Makarova, M., Metzger, J.-M., Morino, I., Murata, I., Nagahama, T., Notholt, J., Ortega, I., Palm, M., Pinardi, G., Röhling, A., Smale, D., Stremme, W., Strong, K., Sussmann, R., Té, Y., van Roozendael, M., Wang, P., and Winkler, H.: TROPOMI–Sentinel-5 Precursor formaldehyde validation using an extensive network of ground-based Fourier-transform infrared stations, Atmos. Meas. Tech., 13, 3751–3767, https://doi.org/10.5194/amt-13-3751-2020, 2020.

Wells, K.C., Millet, D.B., Payne, V.H., Deventer, M.J., Bates, K.H., de Gouw, J.A., Graus, M., Warneke, C., Wisthaler, A., Fuentes, J.D., 2020. Satellite isoprene retrievals constrain

emissions and atmospheric oxidation. Nature 585, 225–233. https://doi.org/10.1038/s41586-020-2664-3

Wolfe, G. M., Kaiser, J., Hanisco, T.F., Keutsch, F.N., de Gouw, J.A., Gilman, J.B., Graus, M., Hatch, C.D., Holloway, J., Horowitz, L.W., Lee, B.H., Lerner, B.M., Lopez-Hilifiker, F., Mao, J., Marvin, M.R., Peischl, J., Pollack, I.B., Roberts, J.M., Ryerson, T.B., Thornton, J.A., Veres, P.R., Warneke, C., 2016. Formaldehyde production from isoprene oxidation across NO_x regimes. Atmospheric Chemistry and Physics 16, 2597–2610. https://doi.org/10.5194/acp-16-2597-2016

Wolfe, Glenn M., Marvin, M.R., Roberts, S.J., Travis, K.R., Liao, J., 2016. The Framework for 0-D Atmospheric Modeling (F0AM) v3.1. Geoscientific Model Development 9, 3309–3319. https://doi.org/10.5194/gmd-9-3309-2016

Xu, W., Zhang, G., Wang, Y., Tong, S., Zhang, W., Ma, Z., Lin, W., Kuang, Y., Yin, L., Xu, X., 2021. Aerosol Promotes Peroxyacetyl Nitrate Formation During Winter in the North China Plain. Environ. Sci. Technol. 55, 3568–3581. https://doi.org/10.1021/acs.est.0c08157

Yang, K., Carn, S.A., Ge, C., Wang, J., Dickerson, R.R., 2014. Advancing measurements of tropospheric NO2 from space: New algorithm and first global results from OMPS. Geophysical Research Letters 41, 4777–4786. https://doi.org/10.1002/2014GL060136

Zhang, K., Duan, Y., Huo, J., Huang, L., Wang, Yangjun, Fu, Q., Wang, Yuhang, Li, L., 2021. Formation mechanism of HCHO pollution in the suburban Yangtze River Delta region, China: A box model study and policy implementations. Atmospheric Environment 267, 118755. https://doi.org/10.1016/j.atmosenv.2021.118755

Zhu, L., González Abad, G., Nowlan, C.R., Chan Miller, C., Chance, K., Apel, E.C., DiGangi, J.P., Fried, A., Hanisco, T.F., Hornbrook, R.S., Hu, L., Kaiser, J., Keutsch, F.N., Permar, W., St. Clair, J.M., Wolfe, G.M., 2020. Validation of satellite formaldehyde (HCHO) retrievals using observations from 12 aircraft campaigns. Atmospheric Chemistry and Physics 20, 12329–12345. https://doi.org/10.5194/acp-20-12329-2020

Zhu, L., Jacob, D.J., Kim, P.S., Fisher, J.A., Yu, K., Travis, K.R., Mickley, L.J., Yantosca, R.M., Sulprizio, M.P., De Smedt, I., González Abad, G., Chance, K., Li, C., Ferrare, R., Fried, A., Hair, J.W., Hanisco, T.F., Richter, D., Jo Scarino, A., Walega, J., Weibring, P., Wolfe, G.M., 2016. Observing atmospheric formaldehyde (HCHO) from space: validation and intercomparison of six retrievals from four satellites (OMI, GOME2A, GOME2B, OMPS) with SEAC^{4}RS aircraft observations over the southeast US. Atmospheric Chemistry and Physics 16, 13477–13490. https://doi.org/10.5194/acp-16-13477-2016

Zhu, L., Jacob, D.J., Mickley, L.J., Marais, E.A., Cohan, D.S., Yoshida, Y., Duncan, B.N., Abad, G.G., Chance, K.V., 2014. Anthropogenic emissions of highly reactive volatile organic compounds in eastern Texas inferred from oversampling of satellite (OMI) measurements of HCHO columns. Environ. Res. Lett. 9, 114004. https://doi.org/10.1088/1748-9326/9/11/114004

Table1. The box model configurations and inputs.

Temporal resolution of samples	10-15 sec
Time steps	1 hour
Number of solar cycles	5
Dilution constant	1/86400 -1/43200 (s^{-1})
Meteorological Inputs	Pressure, Temperature, and Relative Humidity
Photolysis frequencies estimates	LUT based on the NCAR TUV model calculations
Photolysis frequencies constraints (campaign#‡)	Measured jNO_2 (1-4) and jO^1D (4)
Compounds (Instrument#†, campaign#‡) used for constraining the box model	H_2(1, 4)§, CO (4, 1-4), NO_x (2, 1-4), O_3 (2, 1-4), SO_2 (6, 4) , CH_4 (4, 1-4), HNO_3 (10, 1-4), Isoprene (9, 1-4), Monoterpenes (9, 1-4), Acetone (9, 1-4), Ethylene (1, 4), Ethane (1, 4), Methanol (9, 1-4), Propane (1, 4), Benzene (1 or 9, 2-4), Xylene (1 or 9, 1 and 4), Toluene (1 or 9, 1-4), Glyoxal (8, 4), Acetaldehyde (9, 1-4), Methyl vinyl ketone (9, 1-4), Methyl Ethyl Ketone (9, 2-4), Propene (1 or 9, 2 and 4), Acetic acid (9, 2-4), Glycolaldehyde (5, 4), H_2O_2 (5, 4)
Unconstrained compounds (Instrument#†, campaign#‡) used for validation	HO_2 (3, 4), OH (3, 4), NO (2, 1-4), NO_2 (2, 1-4), PAN (10, 1-4), HCHO (7, 1-4)
Chemical Mechanism	CB06

† (1) UC Irvine's Whole Air Sampler (WAS), (2) NCAR 4-Channel Chemiluminescence, (3) Penn State's Airborne Tropospheric Hydrogen Oxides Sensor (ATHOS), (4) NASA Langley's DACOM tunable diode laser spectrometer, (5) Caltech's single mass analyzer, (6) Georgia Tech's ionization mass spectrometer, (7) The University of Colorado at Boulder's the Compact Atmospheric Multi-species Spectrometer (CAMS), (8) Korean Airborne Cavity Enhances Spectrometer, (9) University of Innsbruck's PTR-TOF-MS instrument, and (10) University of California, Berkeley's TD-LIF.

‡ (1) DISCOVER-Baltimore-Washington, (2) DISCOVER-Texas-Houston, (3) DISCOVER-Colorado, and (4) KORUS-AQ

§ In the absence of measurements, a default value of 550 ppbv is specified.

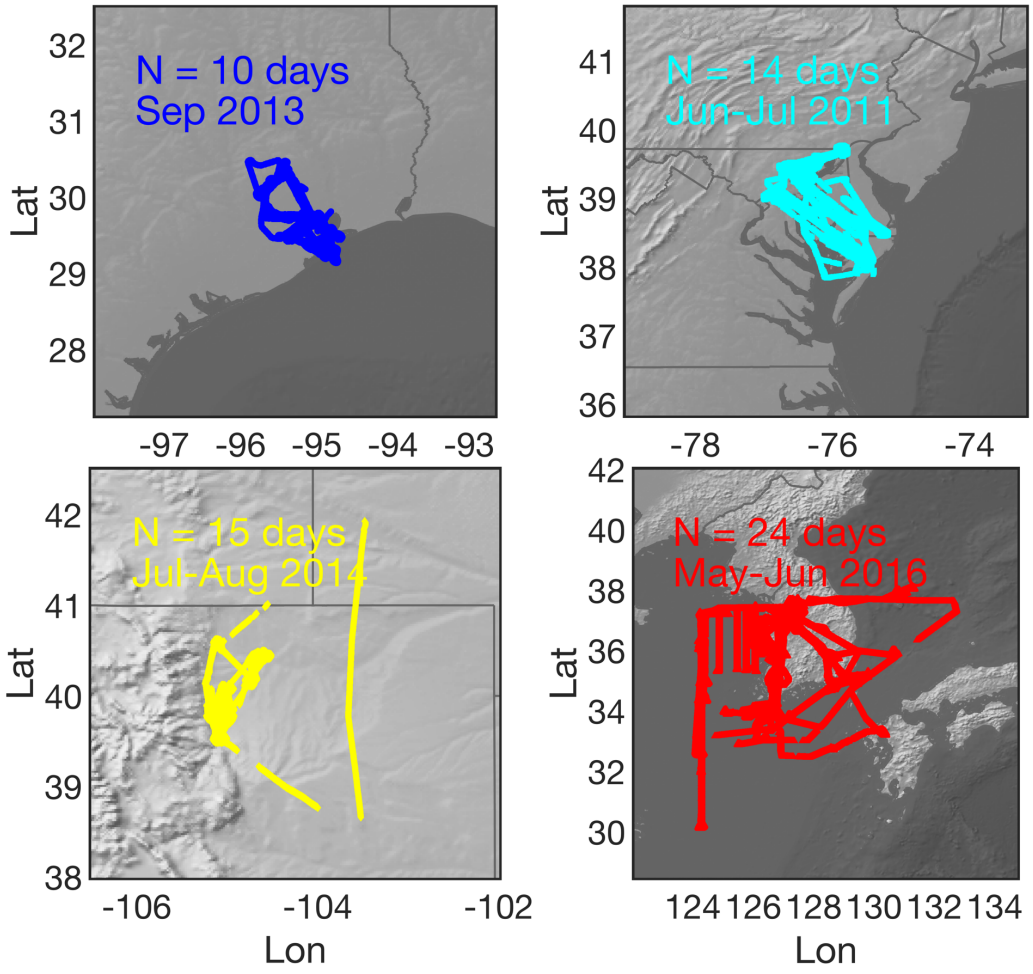

Figure 1. The spatial distributions of aircraft measurements collected during NASA's a) DISCOVER-AQ Houston-Texas, b) DISCOVER-AQ Baltimore-Washington, c) DISCOVER-AQ Colorado, and d) KORUS-AQ. The duration of each campaign is based on how long the aircraft was in the air.

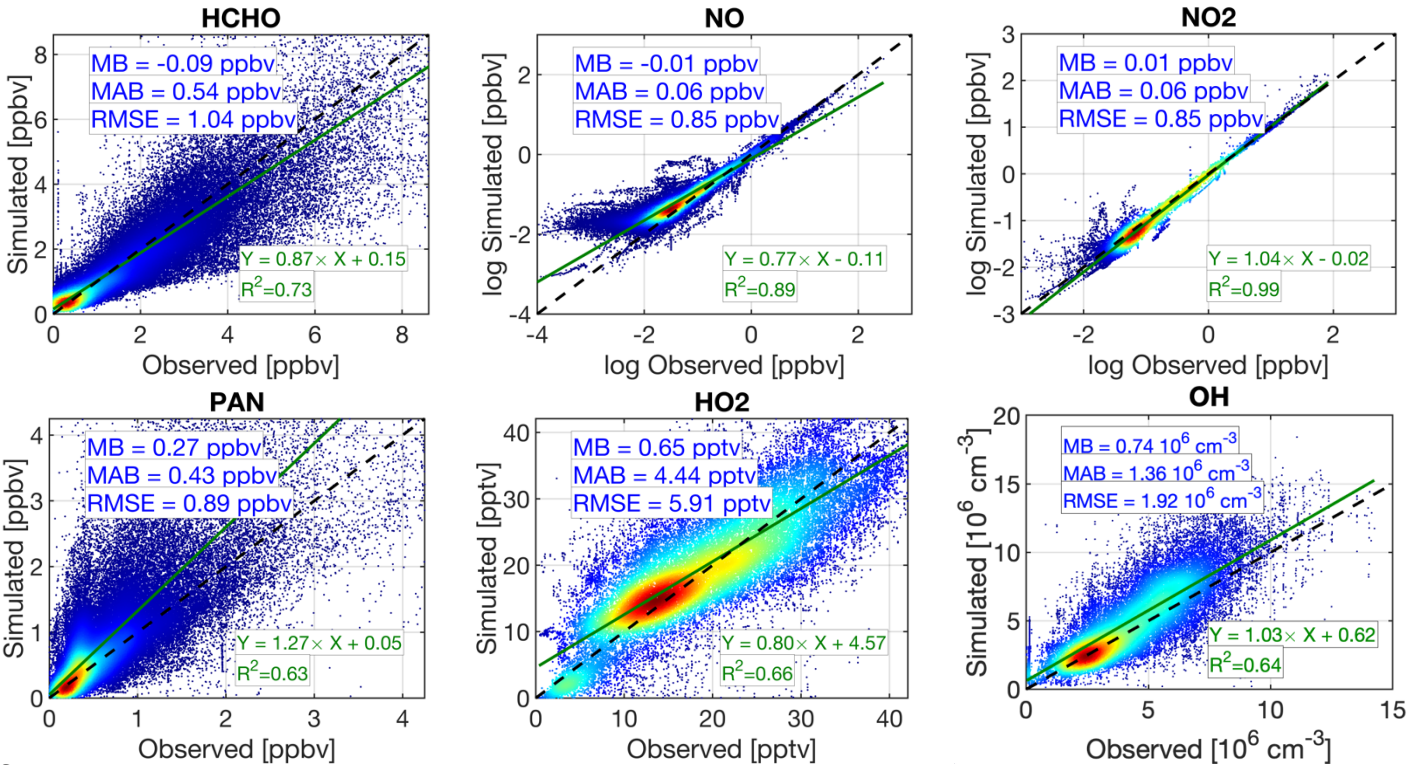

Figure 2. The comparisons of the observed concentrations of several critical compounds to those simulated by our F0AM box model. Each subplot contains mean bias (MB), mean absolute bias (MAB), and root mean square error (RMSE). The least-squares fit to the paired data along with the coefficient of determination (R^2) is also individually shown for each compound. Note that we do not account for the observations errors in the x-axis. The concentrations of NO and NO_2 are log-transformed.

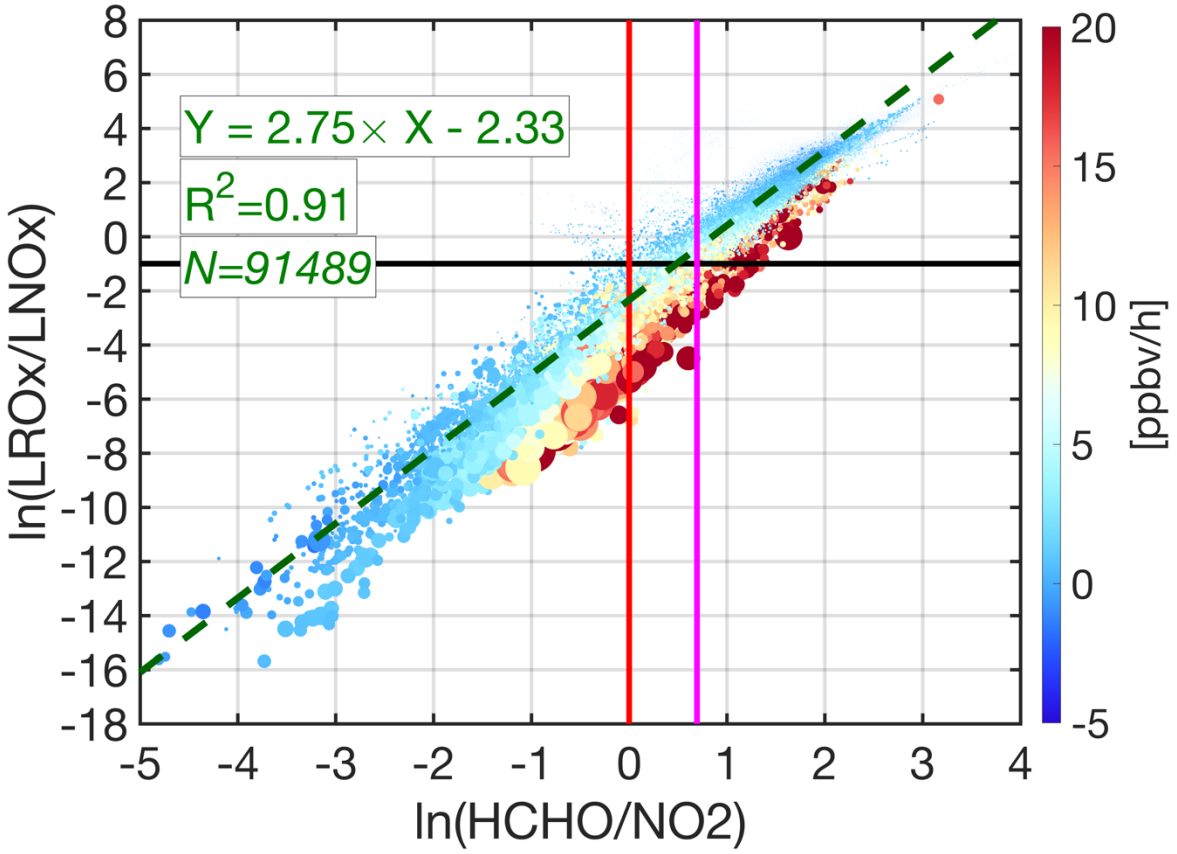

Figure 3. The scatterplot of natural logarithm-transformed of $HCHO/NO_2$ versus LROx/LNOx based on the simulated values performed by the F0AM box model. The heat color indicates the calculated ozone production rates (PO_3). The size of each data point is proportional to $HCHO \times NO_2$. The black line is the baseline separator of NOx-sensitive (above the line) and VOC-sensitive (below the line) regimes. We overlay $HCHO/NO_2=1$ and $HCHO/NO_2=2$ as red and purple lines, respectively. The dashed dark green line indicates the least-squares fit to the paired data. The $HCHO/NO_2 = 1.8$ with 20% error is the optimal transitioning point based on this result.

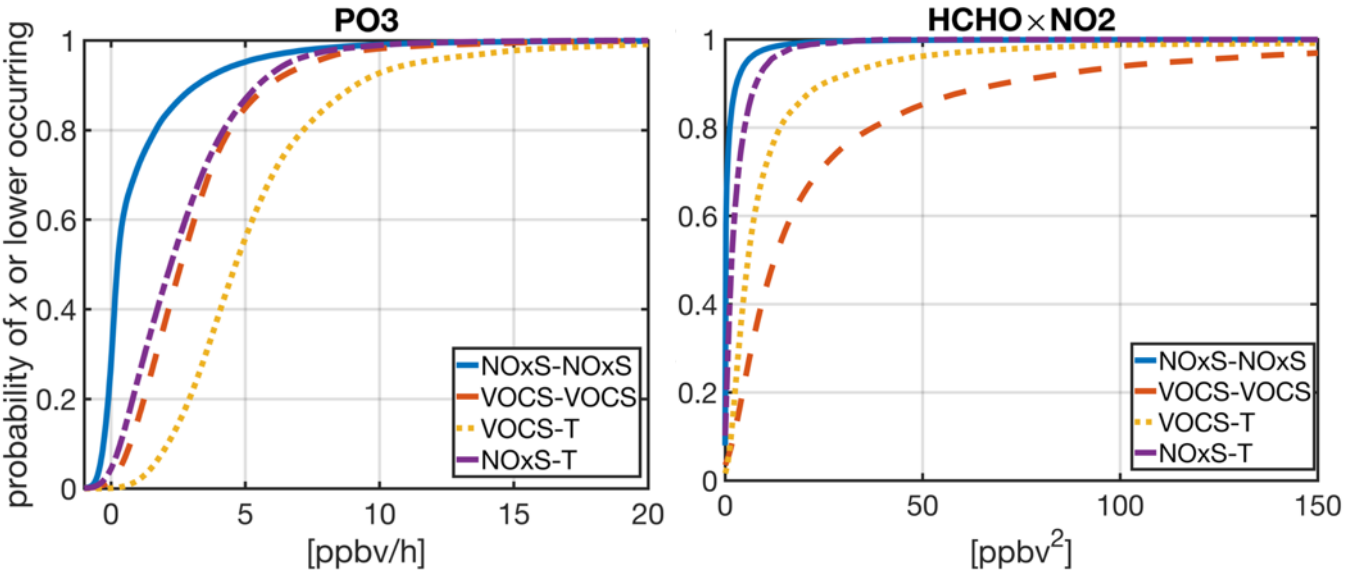

Figure 4. Cumulative distribution functions of PO_3 and $HCHO \times NO_2$ simulated by the box model constrained by NASA's aircraft observations. Four regions namely as NOx-sensitive — NOx-sensitive, NOx-sensitive—transitional, VOC-sensitive—transitional, and VOC-sensitive—VOC-sensitive are shown. The first name of the regime is based on the baseline (ln(LROx/LNOx)=-1.0), whereas the second one follows those defined in Duncan et al. (2010): VOC-sensitive if $HCHO/NO_2<1$, transitional if $1<HCHO/NO_2<2$, and NO_x-sensitive if $HCHO/NO_2>2$.

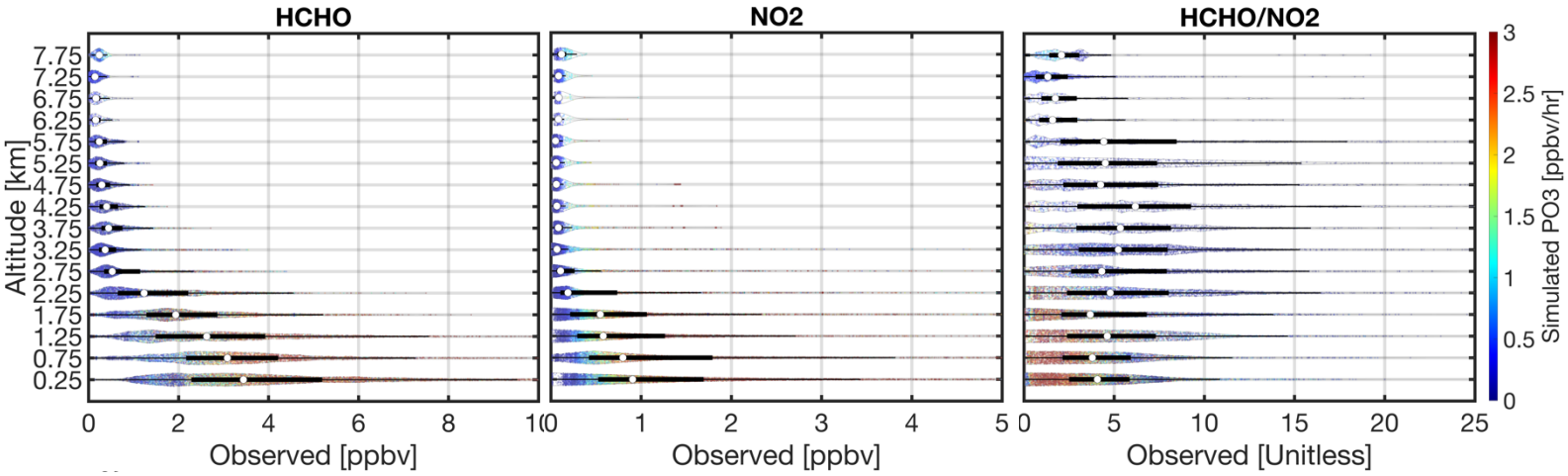

Figure 5. The violin plots of the afternoon vertical distrubution of HCHO, NO_2, and HCHO/NO_2 observations collected during DISCOVER-AQ Texas, Colorado, Maryland, and KORUS-AQ campaings. The violin plots demonstrate the distrubtion of data (i.e., a wider width means a higher frequency). The median is shown by white dots. Both 25th and 75th percentiles are shown by a solid black line. The heatmap denotes the simulated ozone prooduction rates.

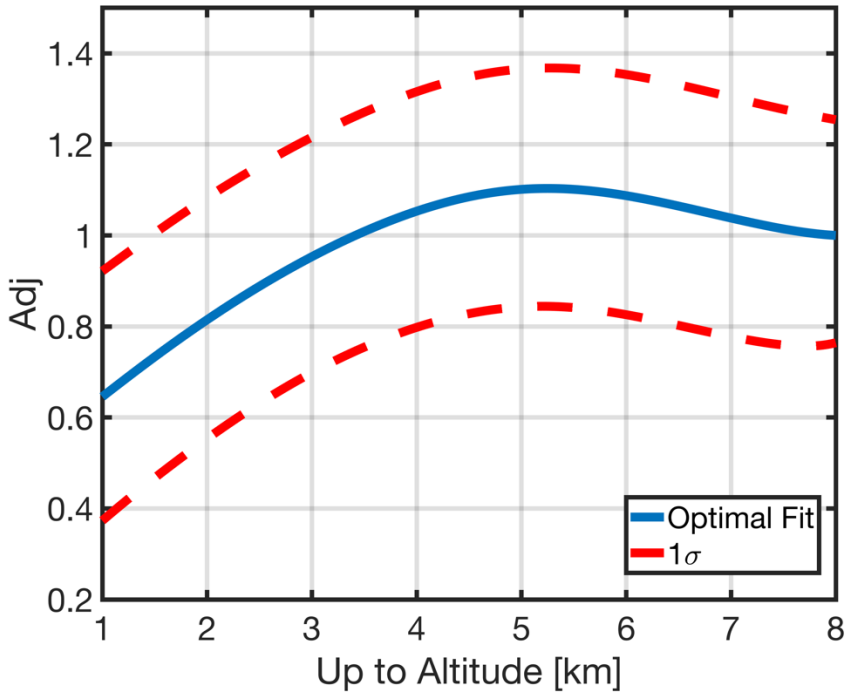

Figure 6. The adjustment factor defined as the ratio of the centriod (first moment) of the polygon bounding 25th and 75th percentiles of the observed HCHO/NO_2 columns by the NASA's aircraft between the surface to 8 km to the ones between the surface and a desired altitude. This factor can be easily applied to the observed HCHO/NO_2 columns to translate the value to a desired altitude stretching down to the surface (i.e., PBLH). The optimal curve follows a quadratic function formulated in Eq11.

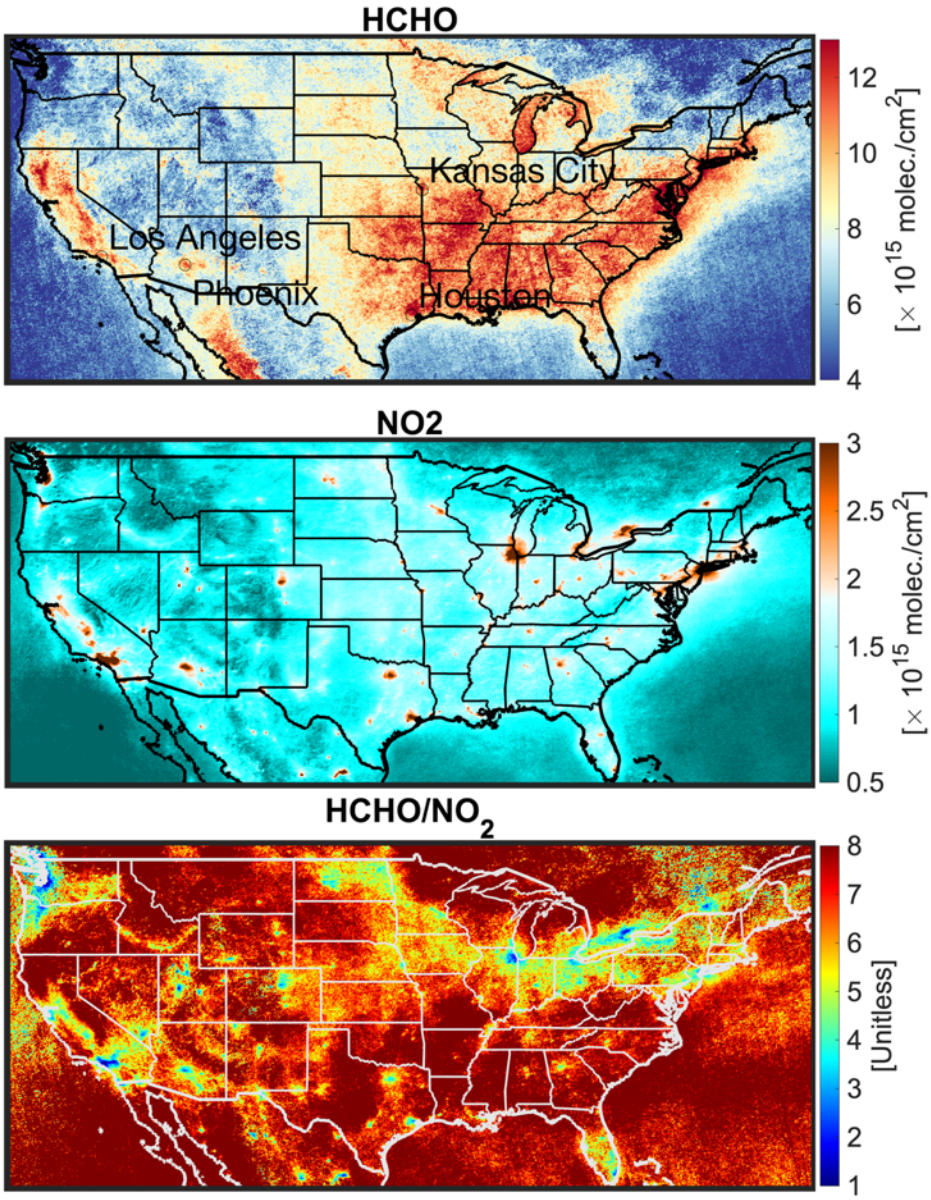

Figure 7. Oversampled TROPOMI total HCHO columns (top), tropospheric NO_2 columns (middle), and the ratio (bottom) at 3×3 km^2 from June till August 2021 over the US.

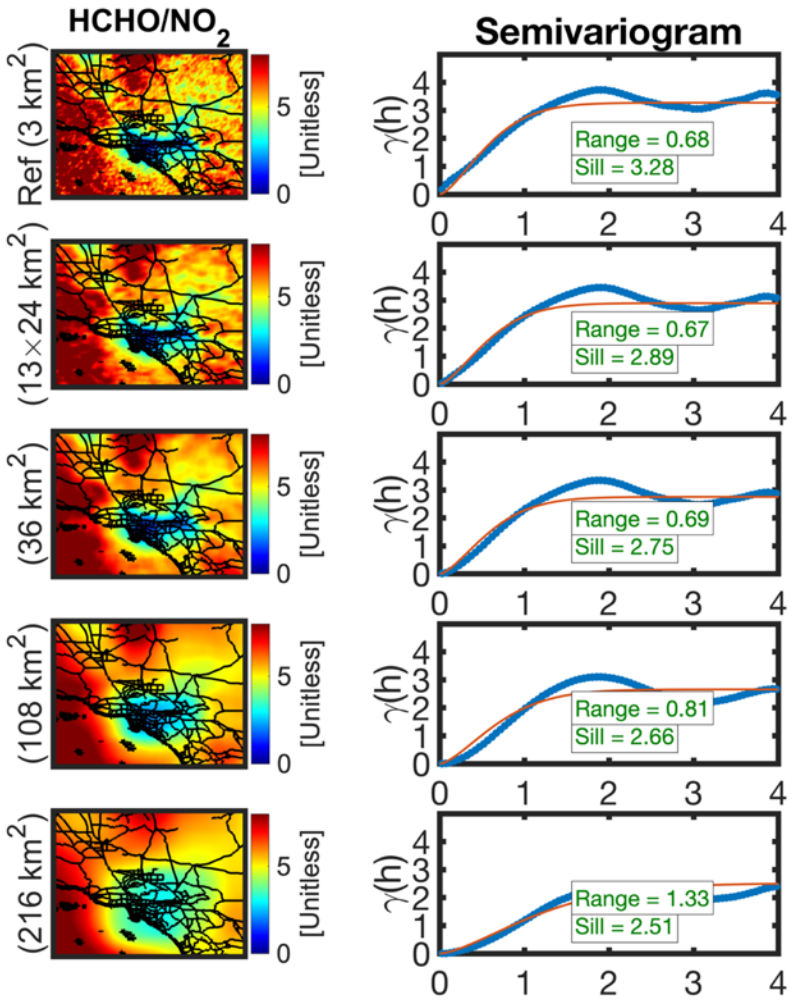

Figure 8. The first column represents the spatial map of $HCHO/NO_2$ ratios over Los Angeles in June till August 2021 at different spatial resolutions. To upscale each map to a coarser footprint, we use an ideal box filter tailored to the target resolution. The second column shows the semivariograms corresponding to the left map along with the fitted curve (red line). The sill and the range are computed based on the fitted curve. The x-axis in the semivariogram is in degree (1 degree ~ 110 km).

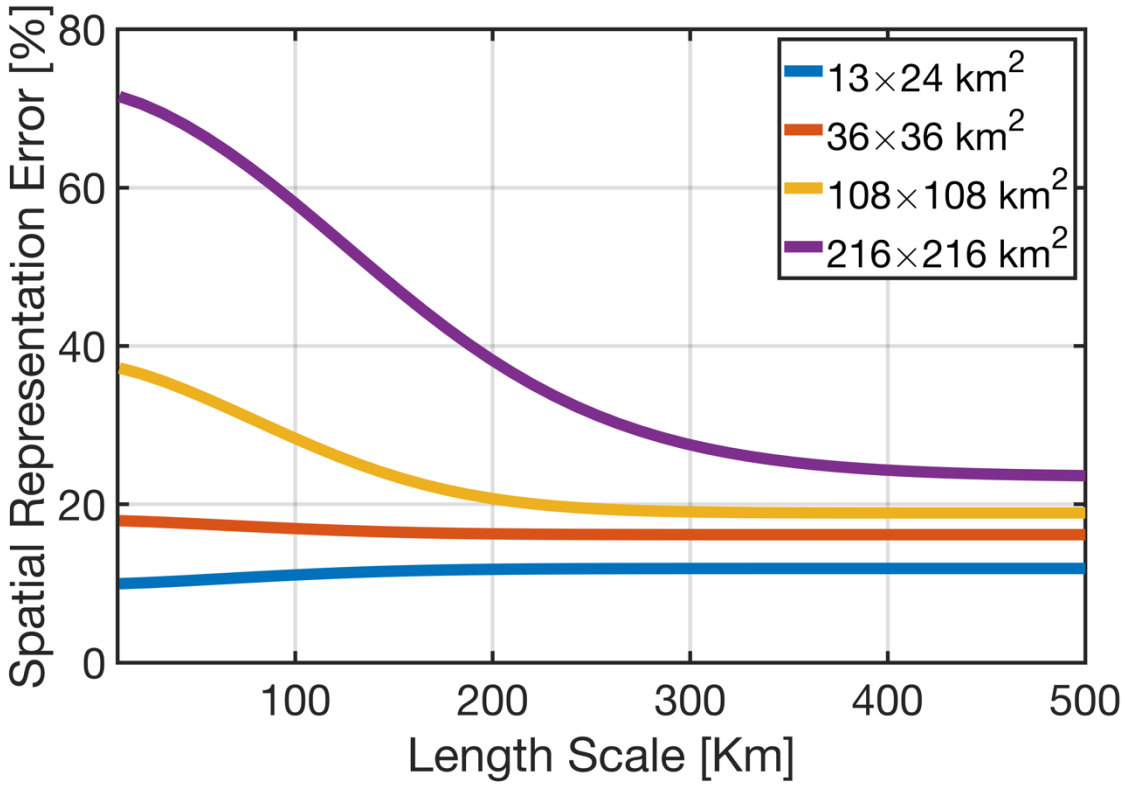

Figure 9. The spatial representation errors quantified based on the proposed method in this study. The error explains the spatial loss (or variance) due to the footprint of a hypothetical sensor at different length scales. To put this error in perspective, a grid box with 216×216 km^2 will naturally lose 65% of the spatial variance existing in the ratio at the scale of Los Angeles which roughly is 50 km wide. All of these numbers are in reference to the TROPOMI 3×3 km^2.

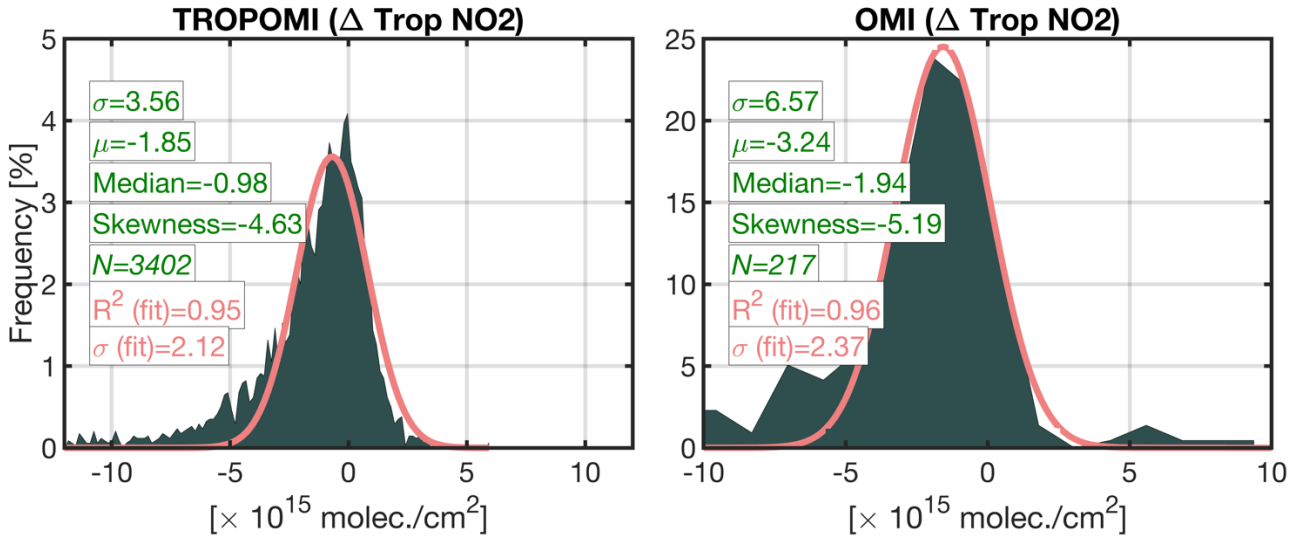

1

1325 **Figure 10.** The histogram of the differences between TROPOMI and OMI and benchmarks. MAX-
1326 DOAS and integrated aircraft spirals are the TROPOMI and the OMI benchmarks, respectively.
1327 The data curation and relevant criteria on how they have been paired can be found in Verholest et
1328 al. (2021) and Choi et al. (2020). The statistics in green color are based on all data, whereas those
1329 in pink are based on the fitted Gaussian function.
1330

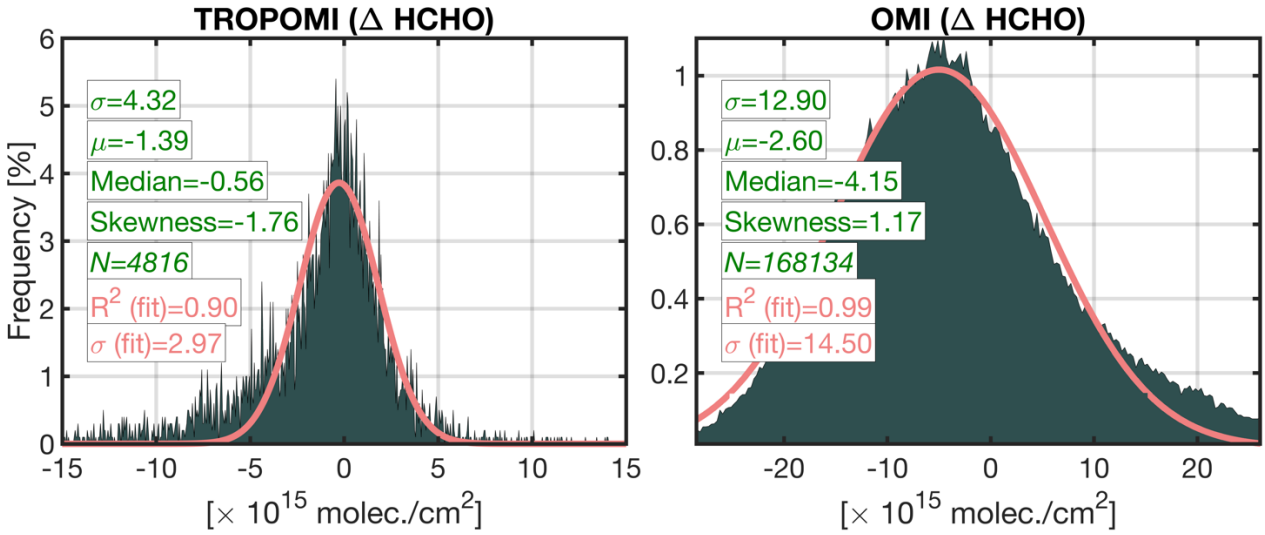

13

1332 **Figure 11.** The histogram of the differences between TROPOMI and OMI and benchmarks. FTIR
1333 and corrected GEOS-Chem simulations are respectively the TROPOMI and the OMI benchmarks.
1334 The data curation and relevant criteria on how they have been paired can be found in Vigouroux
1335 et al. (2021) and Zhu et al. (2020). The statistics in green color are based on all data, whereas those
1336 in pink are based on the fitted Gaussian function.
1337
1338

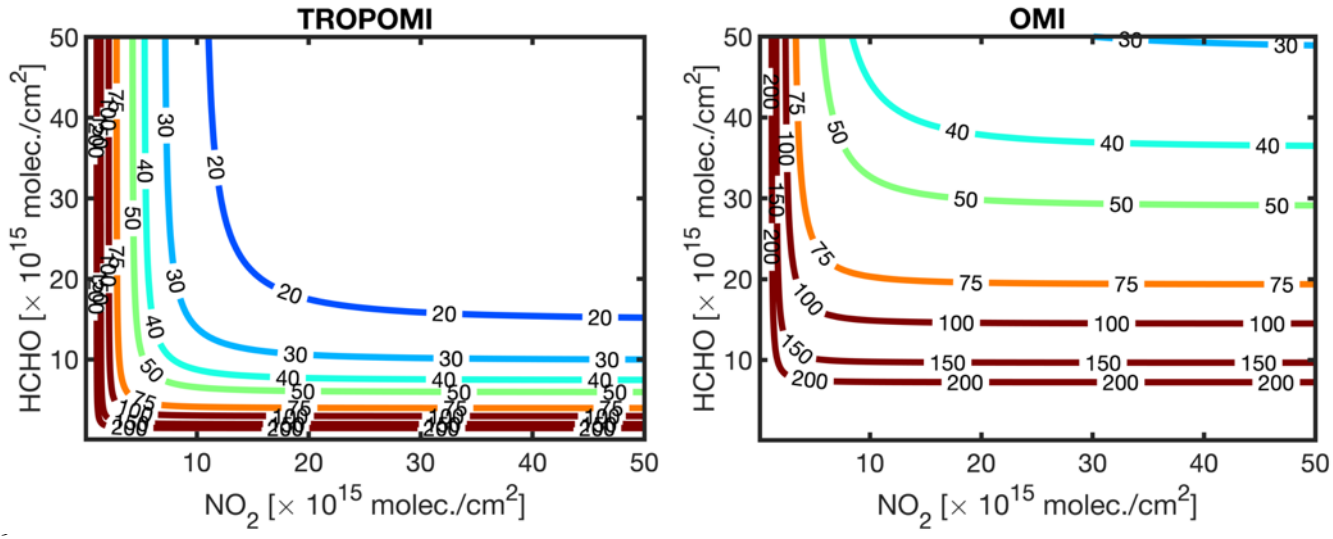

Figure 12. The contour plots of the relative errors in TROPOMI (left) and OMI (right) based on dispersions derived from Figure 10 and 11. The errors used for these estimates are based on daily observations.

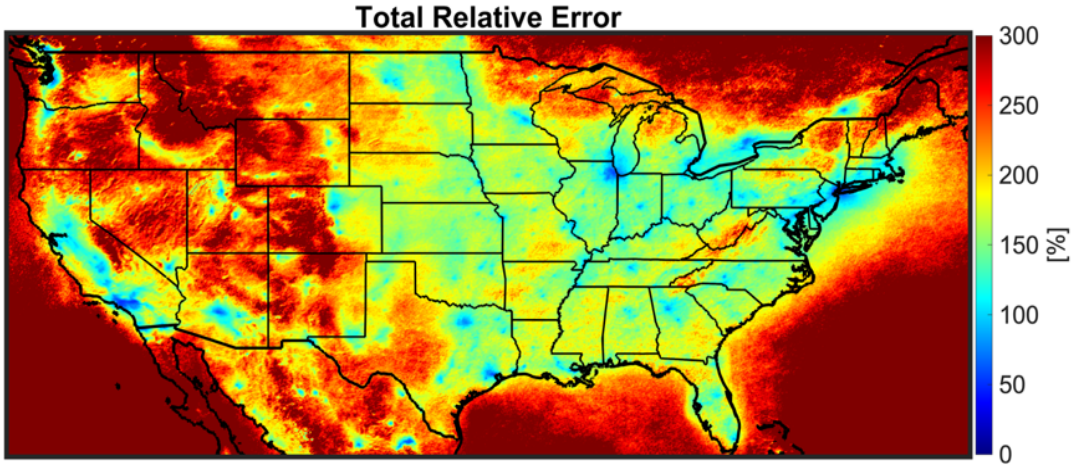

Figure 13. The total relative error for observed TROPOMI HCHO/NO_2 ratios considering the daily TROPOMI retrieval errors (σ_{NO_2}= 2.11×10^{15} molec./cm^2 and σ_{HCHO}= 2.97×10^{15} molec./cm^2), the spatial representation pertaining to OMI footprint over a city environment (13% loss in the spatial variance), and the column to the PBL translation parameterization (26%) proposed in this study. Please note that the observed FNR is based on mean values from June till August 2021, while the uncertainties used for error calculation are on daily-basis.

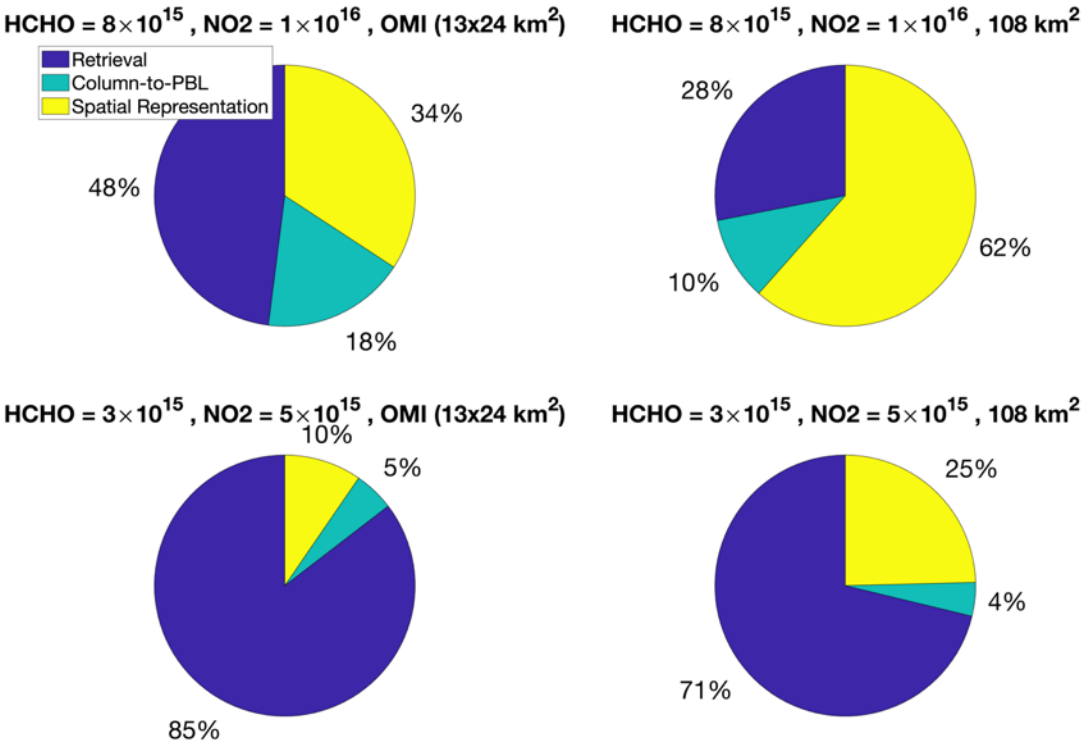

Figure 14. The fractional errors of retrieval (blue), column to PBL translation (green), and spatial representation (yellow) of the total error budget for different concentrations and footprints based on TROPOMI sigma values. The retrieval error used for the error budget is on daily basis.

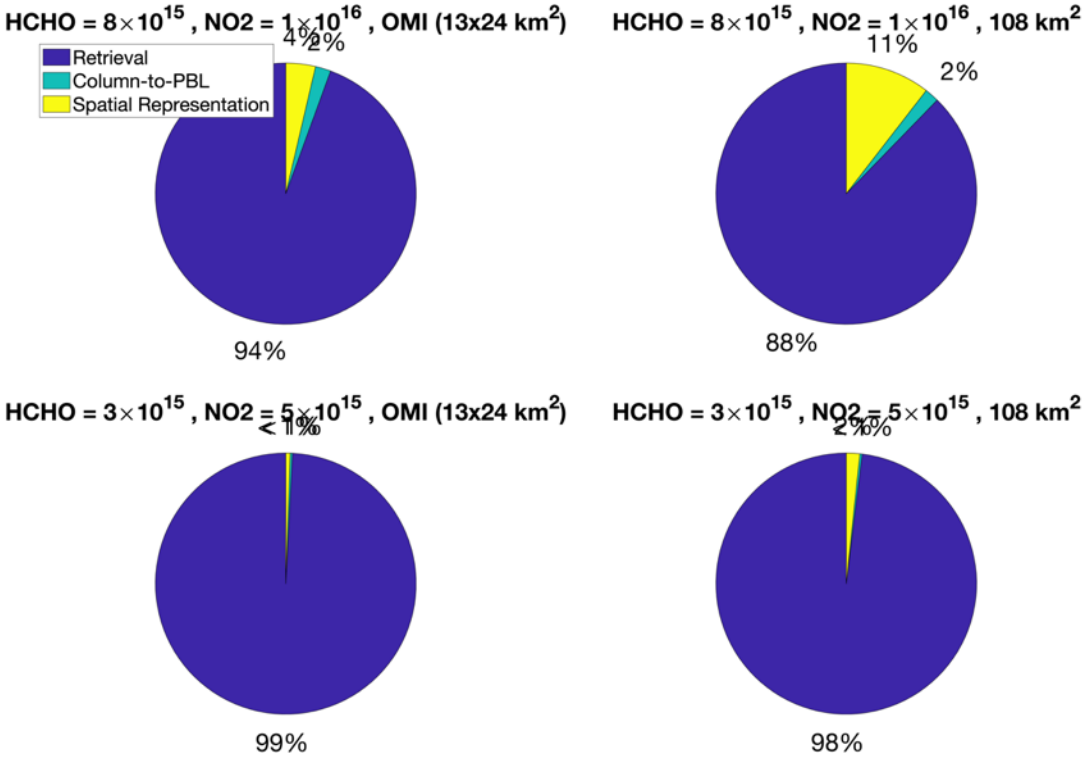

Figure 15. Same as Figure 14 but based on OMI sigma values.